Chapter 3

SCRF Linac Technology

3.1 Overview of the ILC Main Linacs

3.1.1 Overview

The two main linacs accelerate the electron and positron beams from their injected energy of 15 GeV to their final collision energy of between 100 GeV and 250 GeV, over a combined length of 22 km. The linacs utilise approximately 16,000 L band (1.3 GHz) superconducting technology, with nine-cell standing-wave niobium cavities operating at an average gradient of 31.5 MV/m in a 2 K superfluid helium bath, integrated into ∼1,700 12 m long cryomodules. The choice of operating frequency is a balance between the higher cost of larger, lower frequency cavities and the increased cost at higher frequency associated with the lower sustainable gradient from the increased surface resistivity. The optimum frequency is in the region of ∼1.5 GHz, but during the early R&D on the technology, 1.3 GHz was chosen due to the commercial availability of high power klystrons at that frequency [1].

Table 3.1. Cavity performance specifications for the ILC main linacs.

	Gradient MV/m				min. Q_0
	min	average	max	rel. spread	
Operational accelerating gradient	25.2	31.5	37.8	±20%	1×10^{10}
Low-power vertical test	28	35	42	±20%	8×10^{9}

The TESLA elliptical cavity has been chosen for the ILC baseline design due to its maturity, cost effectiveness, and the experiences accumulated over the past decade and a half. In particular, approximately 800 TESLA cavities are currently under production for the European XFEL. Table 3.1 summarises the performance specifications of the cavities for the ILC main linacs. An average accelerating gradient 31.5 MV/m is required for 500 GeV centre-of-mass-energy operation. However, the main linac systems — and in particular the RF power systems — are specified to accommodate up to a ±20% spread in individual cavity performance. The initial low-power vertical test (mass production acceptance test) is specified ∼ 10% higher to allow for operational gradient overhead for low-level RF (LLRF) controls, as well as some degradation during cryomodule installation (few MV/m).

The design average acceleration gradient and qualify factor ($Q_0 = 10^{10}$) has been achieved and exceeded in many cavities, several of which accelerate beam in the TTF/FLASH facility at DESY, Hamburg (see Part I Section **??**). Mass production of high-performance cavities by industry has progressed significantly in the last years, and there is confidence that the required parameters can be achieved (see Part I Section **??**).

The cryomodule is a similar in design to that developed by the TESLA collaboration, of which over ten examples have been constructed, six of which are operational at TTF/FLASH. For the ILC, two types of modules are foreseen, one integrating nine cavities (Type-A), and one integrating integrating eight cavities, with a superconducting quadrupole package located at its centre of the string (Type-B). Both modules are designed to have the identical length of 12.63 m.

3.1.2 Linac layout

Table 3.2 provides an overview of the main parameters and component counts for the ILC main linacs. The linacs are constructed from a near contiguous string of cryomodules, interrupted only by the segmentation of the cryogenic strings (see below). The linacs are housed in underground tunnels which follow the curvature of the earth, primarily to simplify the flow of the two-phase helium at 2 K. The electron linac has an additional nine cryomodules to provide the ~ 2.6 GeV needed to compensate the energy loss in the the undulator-based positron source (Section **??**). In addition both electron and positron linacs have $\sim$1.5% energy overhead for reliability.

Either 26 or 39 adjacent cavities are effectively driven by a common RF power source as indicated in Fig. 3.1. The local power distribution system provides flexibility in adjusting the forward power to each cavity, necessary in dealing with the expected spread in individual cavity gradient performance (see Section 3.6.4). The RF power is provided by 10-MW multi-beam klystrons driven by a solid-state Marx modulator (see Section 3.6.3 and Section 3.6.2 respectively).

Two possible schemes (flat and mountain topography respectively) have been developed during the Technical Design Phase for the layout of the tunnels, and in particular the approach to delivering RF power from the klystrons to the local distribution system and ultimately the cavities:

- For a *mountain topography*, such as the candidate sites in Japan, the more standard Distributed Klystron Scheme (DKS) would be used in a 11 m-wide, "kamaboko-shaped" tunnel whose interior is divided into two corridors by a thick (2.0 m to 3.5 m) concrete wall. The cryomodules occupy one side of the tunnel while the RF system including modulators, klystrons, power supplies, and instrumentation racks, are located on the other side. This arrangement permits access to the equipment on the RF source side for maintenance, repair, or replacement during beam operation, and limits radiation exposure to most of the electronics (except for motors in or near the cryomodules).

- For a *flat topography*, a novel Klystron Cluster Scheme (KCS) is envisioned, with all RF generating equipment located in surface facilities where the klystron

Table 3.2. Summary of key numbers for the SCRF Main Linacs for 500 GeV centre-of-mass operation. Where parameters for positron and electron linacs differ, the electron parameters are given in parenthesis.

Cavity (nine-cell TESLA elliptical shape)		
Average accelerating gradient	31.5	MV/m
Quality factor Q_0	10^{10}	
Effective length	1.038	m
R/Q	1036	Ω
Accepted operational gradient spread	±20%	
Cryomodule		
Total slot length	12.652	m
Type A	9 cavities	
Type B	8 cavities	1 SC quad package
ML unit (half FODO cell)	282 (285)	units
(Type A - Type B - Type A)		
Total component counts		
Cryomodule Type A	564 (570)	
Cryomodule Type B	282 (285)	
Nine-cell cavities	7332 (7410)	
SC quadrupole package	282 (285)	
Total linac length – flat top.	11027 (11141)	m
Total linac length – mountain top.	11072 (11188)	m
Effective average accelerating gradient	21.3	MV/m
RF requirements (for average gradient)		
Beam current	5.8	mA
beam (peak) power per cavity	190	kW
Matched loaded Q (Q_L)	5.4×10^6	
Cavity fill time	924	µs
Beam pulse length	727	µs
Total RF pulse length	1650	µs
RF to beam power efficiency	44%	

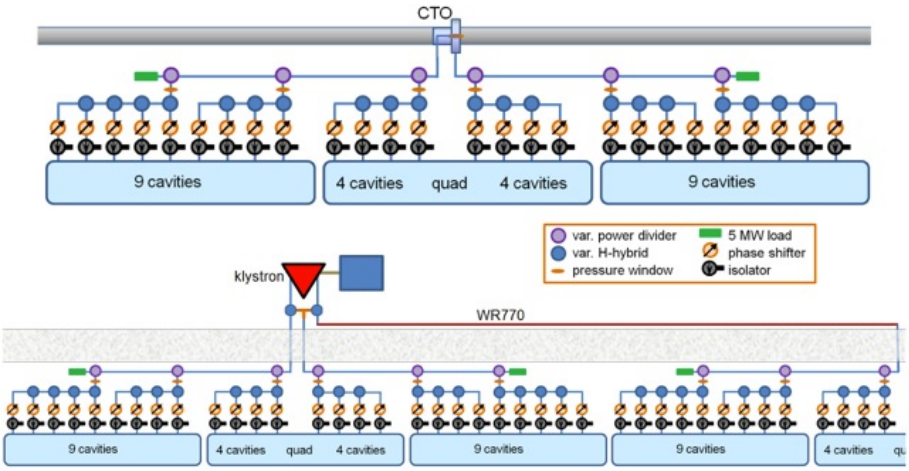

Figure 3.1. Schematic of the Local Power Distribution System (LPDS) which delivers RF power to accelerating cavities in the main linacs. (a) shows the case of the KCS option, and (b) shows the case of the DKS option. In both cases each LPDS input feed drives 13 cavities. (**Ed:** *NT: Please touch up the figure and add labels (a) and (b).)*

power is combined (up to 300 MW) and transferred through over-sized circular waveguides to the linac tunnel below. The tunnel, which is about 5 m in diameter, mainly contains the cryomodules and waveguides with some electronics (e.g., quadrupole magnet power supplies and LLRF monitoring and control electronics) that is housed in radiation shielded, 2 m-wide racks under the cryomodules.

The tunnels are assumed to be deep underground (∼100 m) and connected to the surface through vertical shafts (flat sites) or sloped access routes (mountain sites). The number, location and size of these shafts or access ways is determined by the maximum length of a cryogenic unit (and maximum available size of a cryoplant, see below), and in the case of KCS the maximum distance over which the RF power can be realistically transported via the large over-moded circular waveguide (Section **??**).

The cryogenic segmentation (layout) of the main linacs is divided into the following units:

- An **ML unit** with consists of three cryomodules in a Type A – Type B – Type A arrangement (26 cavities and 1 quadrupole package);
- A **cryo string**, which consists of 4 ML units (long string with 12 cryomodules) or 3 ML units (short string with 9 cryomodules), followed by a 2.5 m cold-box;
- A **cryo unit** comprising of between 10 to 16 cryo strings, with the final cold-box being replaced by an 2.5 m service box.

Fig. 3.2 shows an example configuration for a single cryo unit based on 13 long cryo strings. The maximum length for a cryo unit is approximately 2.5 km, and is set by consideration of the largest practical cryoplant size (approximately 4 MW,

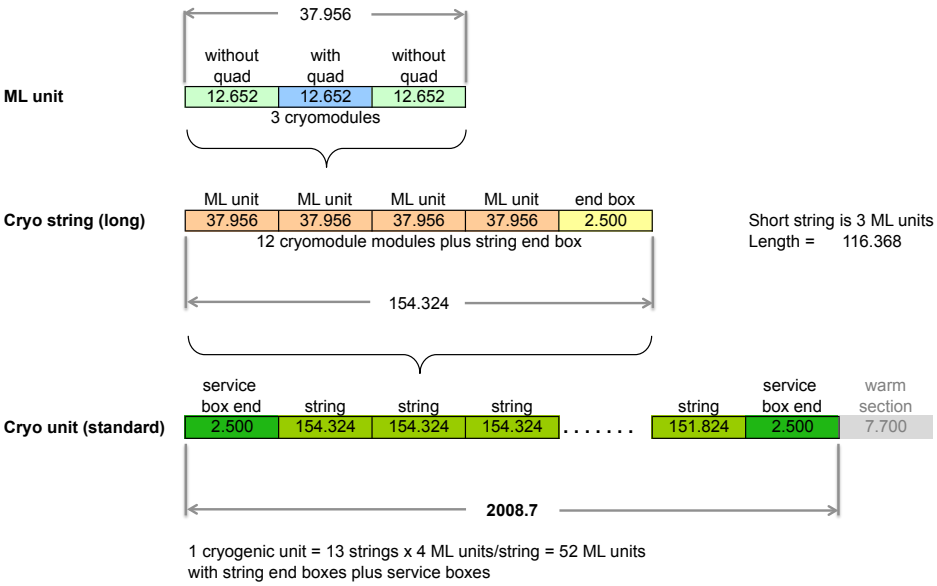

Figure 3.2. Basic cryogenic segmentation in the main linacs. Note that the lengths of the cryo units varies depending on the number of strings. (All lengths given in metres.)

comparable to those running at LHC). This includes a 40% overcapacity to account for degradation of plant performance, variation in cooling water temperature, and operational overhead. (About half of the AC power consumed in the cryoplants is used to remove the RF energy dissipated in the 2 K cavities.) Two cryoplants are typically located together, with one plant feeding an upstream cryo unit and the other a downstream cryo unit. This results in a typical spacing of cryo plant installations (vertical shafts or access ways) of approximately 5 km. The most upstream cryoplant also provides cooling for the accelerator sections for the bunch compressors in the RTMLs (Chapter **??**). The exact linac segmentation and number of cryoplants differs for the two site-dependent variants considered, although the number of cryomodules in the linacs are the same. In particular, five cryoplants are envisaged for the mountainous topography, while for the flat topography the total load is distributed over six plants. These differences are driven by the approach to the RF power distribution for each site variant. Chapter **??** and Chapter **??** provide details of the main linac segmentation for the flat and mountainous topographies respectively.

Each cryo unit is separated by a short ∼7.7 m warm section that includes vacuum system components and a 'laser wire' to measure beam size. Accounting for these additional sections, the active to actual length ratio in the linacs is 69%.

At the exit of main linacs there is a section of warm beamline which acts as the matching interface to the downstream systems. This section of beamline will provide:

- Matching and machine protection collimation for transitioning between the relative large apertures in the main linac, to the smaller ones in the downstream

(warm) systems (most notably the positron source undulator located at the exit of the electron linac).

- Beam trajectory correction using a fast intra-train feedback/feedforward system, which should reduce pulse to pulse jitter to approximate 10% of the vertical beam height. The fast kickers will also be used to correct repetitive bunch to bunch variation possibly arising from long-range wake fields (so-called 'beam straightener'). On the electron linac side, in addition to the fast feedback correction, a 10 Hz pulse magnet system is required to adjust the 150 GeV positron production beam during 10 Hz mode operation at low centre-of-mass operation.

Conventional cooling provided by surface cooling towers located at the primary shafts or access ways. Through various distribution loops, the cooling towers provide 35 °C 'process' water that removes most of the heat generated by the RF system, and 8 °C 'chilled' water for heat exchangers that maintain the tunnel air temperature at 29 °C and cool electronics racks via closed, circulated-air systems.

Table 3.3 summarizes the combined power consumption of the Main Linacs. Of this power, 9.9 MW goes into the beams and the corresponding wall-plug power to beam power efficiency is 9.6%.

Table 3.3. Main Linac AC power consumption for both site-dependent variants. Details can be found in Chapter **??**

System	Flat Topography AC power (MW)	Mountain Topography AC power (MW)
Modulators	58.1	52.1
Other RF system and controls	5.8	5.5
Conventional facilities	13.3	13.1
Cryogenics	32.0	32.0
Total	109.2	102.7

3.1.3 Accelerator Physics

Table 3.4 lists the basic beam parameters for the main linacs. The main linac lattice uses FODO optics, with a quad spacing of 37.96 m, corresponding to one quad per three cryomodules (ML unit). Each quadrupole magnet is accompanied by horizontal and vertical dipole correctors and a cavity BPM which operates at 1.3 GHz. The lattice functions are not perfectly regular due to the interruptions imposed by the cryogenic system, but do not change systematically along the linac so the focusing strength is independent of beam energy. Fig. 3.3 shows the lattice for the last cryo-unit of the main linac. The average lattice beta function is approximately 80 m and 90 m in the horizontal and vertical planes respectively. The mean phase advance per cell is 75° in the horizontal plane and 60° in the vertical plane. The small vertical bending required to follow the Earth's curvature is provided by vertical correctors near the quadrupole locations, and gives rise to ∼1 mm of vertical dispersion (peak). Dispersion matching and suppression at the beginning and end of the

Table 3.4. Nominal Linac Beam Parameters for 500 GeV CMS operation.
(**Ed:** *NW: check emittance: original number was 35nm which is now quoted at IP. I have set it to 30nm in this table. Will add additional information (such as typical beam sizes (initial/final) etc.)*

Parameter	Value	Unit
Initial beam energy	15	GeV
Final (max.) beam energy	250	GeV
Particles per bunch	2.0×10^{10}	
Beam current	5.8	mA
Bunch spacing	554	ns
Bunch train length	727	µs
Number of bunches	1312	
Pulse repetition rate	5	Hz
Initial $\gamma\epsilon_x$	8.4	µm
Final $\gamma\epsilon_x$	9.4	µm
Initial $\gamma\epsilon_y$	24	nm
Final $\gamma\epsilon_y$	30	nm
σ_z	0.3	mm
Final $e^-\sigma_E/E$	1.6	%
Final $e^+\sigma_E/E$	0.11	%
Bunch phase relative to RF crest	5	degrees

linac are achieved by supplying additional excitation to small numbers of correctors in "dispersion-bump" configurations.

The beam emittance at the damping ring extraction is $\gamma\epsilon_x = 8\,\mu\text{m}$ and $\gamma\epsilon_y = 20\,\text{nm}$. The biggest challenge is in keeping the small vertical emittance from being degraded during the beam transport to the beam interaction point (IP). This cannot be done perfectly, and the ILC parameters specify a target emittance at the IP of $\gamma\epsilon_x = 10\,\mu\text{m}$ and $\gamma\epsilon_y = 35\,\text{nm}$. An emittance growth budget has been set at $\Delta\epsilon_y \leq 10\,\text{nm}$ for the total of the RTML and the main linac. The goal for the alignment and tuning procedures is to ensure that the emittance growth is within the budget.

To limit the emittance dilution, the position and orientation of the beamline elements are set fairly precisely during installation (Table 3.5), and beam-based alignment methods are then used to adjust the corrector magnet strengths to establish an orbit that minimises the beam emittance growth. The task is made easier by the fact that the long-range (bunch-to-bunch) wakefields are weak and the initial bunch trajectories are very similar, so minimising the emittance growth of one bunch will do this for all bunches. Any slow variation of the relative trajectories of the bunches along the trains will be removed after the linacs using a fast-kicker-based feedback system.

The relatively weak single-bunch longitudinal wakefield also means that only a small off-crest phase (5 degree at 31.5 MV/m) is required to compensated it

To suppress any resonate buildup of the wakefields or their effect on the beam, a higher-order-mode (HOM) damping system has been carefully design into the cavities and the HOM frequencies are effectively detuned cavity-to-cavity at the 10^{-3} level as a result geometric differences within the fabrication tolerances. Such fabrication variations can also lead to diagonal polarisation of the dipole modes

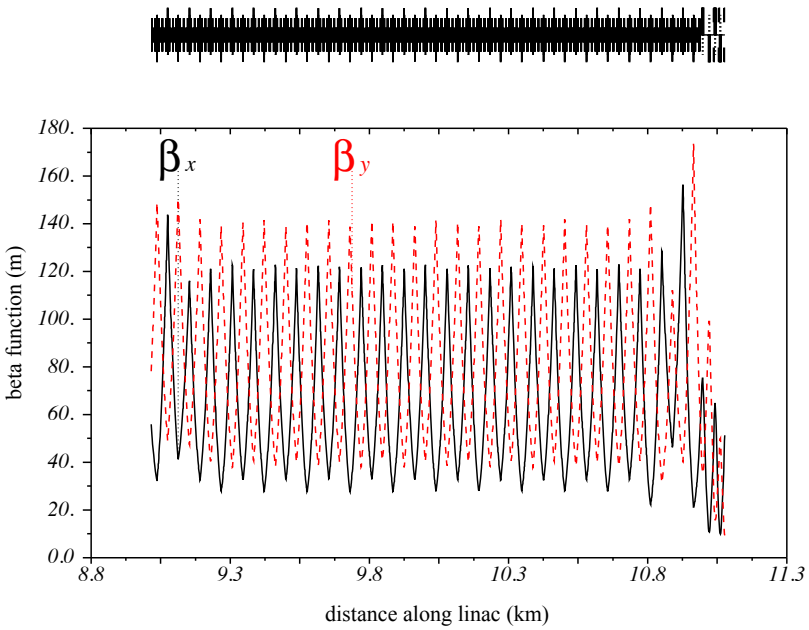

Figure 3.3. Example lattice functions for the main linac. The plot shows the beta functions for the last cryo-unit of the linac. (The warm post-linac collimation system is also included.)

instead of horizontal and vertical polarisation. The difference in horizontal and vertical betatron phase advance noted above prevents such mode x-y coupling from causing orbit jitter to couple between the horizontal and vertical planes.

(**Ed:** *NJW: Need to discuss what to include in this chapter on the HOM issue. Most of this work was done 10 years ago for TESLA. A table of the modes is given in the TESLA TDR, as well as results of multi-bunch simulations, but this never been reproduced in any document for the ILC. Effectively this field has been considered a "solved problem" for many years. What should we do for this TDR? Reproduce some of this? At the very least we should reference the work done for TESLA.)*

Table 3.5. Installation alignment errors (rms) the linac beamline elements.

Error	with respect to	value	
Cavity offset	module	300	µm
Cavity tilt	module	300	µrad
BPM offset	module	300	µm
Quadrupole offset	module	300	µm
Quadrupole roll	module	300	µrad
Module offset	beamline reference	200	µm
Module tilt	beamline reference	20	µrad

The assumed installation errors are listed in Table 3.5. Cavities and Quadrupole magnets are inaccessible once installed into the cryomodules, and need to be mounted and carefully aligned during assembly in a way to allow for thermal contractions of the support system during the cryostat cool down. Results of stretched wire mea-

surements in cryomodules at DESY have demonstrated that the specifications can be reproducibly met over several thermal cycles [**?**]. After installation in the tunnel, the offsets of the quadrupole and BPM are ultimately established by beam-based techniques at the micron level (i.e., the quadrupole centres are shifted with corrector magnets and the BPM offsets are determined with a quadrupole shunting technique). The bunch emittance dilution is dominated by chromatic (dispersive) effects and wakefield kicks arising from misaligned quadrupole magnets and cavities respectively. Emittance growth from these perturbations are mainly corrected through local or quasi-local steering algorithms such as Ballistic Alignment (BA), Kick Minimisation (KM), or Dispersion Free Steering (DFS), with additional correction achieved through local orbit distortions, which produce offsetting amounts of dispersion at a given phase ('dispersion bumps'). A more complete description of the emittance dilution mechanisms and the steering algorithms be can found in Part I Section **??**.

A BPM with horizontal and vertical readout and micron-level single-bunch resolution is located adjacent to each quadrupole magnet. For beam size monitoring, a single laser wire is located in each of the warm sections between main linac cryogenics units (about every 2.5 km). Upstream quadrupole magnets are varied to make local measurements of the beam emittances at these points.

3.1.4 Operation

Fast trajectory control is implemented in the warm regions upstream and downstream of the Main Linacs but not within the linacs themselves, as the trajectory jitter generated by magnetic and RF field variations is expected to be small (see Part I Section **??**). Likewise, beam energy and energy spread are only measured upstream and downstream of the Main Linacs, and there are no beam abort systems or energy collimation chicanes along the linacs. The Machine Protection System will only allow beam into the RTML if the trajectory is within a defined phase space, and if the RF phases in the RTML and Main Linac cavities are within a prescribed range prior to the beam extraction from the damping rings (during the approximately 800 µs fill time for the RF). The limiting aperture in the cryomodules are the 70 mm diameter cavity irises, which provides a safe beam stay clear.

The linac length (number of cryomodules) includes a 1.5% energy overhead for 250 GeV operation. This overhead allows some loss in energy gain due to failed cavities or RF systems. (See Section **??** for more details.)

The required beam energy is first 'coarsely' adjusted by setting the required RF power and cavity Q_{ext}, and 'finely' adjusted by cross-phasing RF units near the end of the linacs. (**Ed:** *NW note that this type of SLC-like beam feedback is not accounted for in the length. Part of the 1.4%?)* For low beam-energy operation (low gradient), the modulator voltage and RF pulse length would be reduced to save energy or to allow for a higher pulse rate operation, as would be needed for 10 Hz mode positron production mode for $E_{CM} \leq 250$ GeV.

3.1.5 Linac Systems

The remaining sections of this chapter describe in detail the main components of the Main Linacs, starting from the SC cavities and working outward through the cryomodule, high power RF systems and finally to the low-level RF (LLRF) controls:

Section 3.2 Cavity performance and production specifications covers the cavity design, performance specifications, and baseline industrial production process, including the required surface preparation to achieve the required high-performance.

Section 3.3 Cavity integration discusses the complete cavity package and how it is assembled, including the high-powerRF coupler, HOM couplers, helium tank and mechanical frequency tuner.

Section 3.4 Cryomodule design including quadrupole and cryogenic systems describes the mechanical design of the 12.7 m long cryomodules, which comprise the vacuum vessel and the items within including cavities, thermal shielding, cryogenic feed and return lines, beamline absorber and a quad 'package,' consisting of a quadrupole magnet, horizontal and vertical corrector magnets and an RF BPM. Estimates of the cryogenic heat loads are also presented.

Section 3.5 Cryogenic cooling system describes the layout of the cryogenic plants and required plant capacities. (**Ed:** *THIS IS NEW - copied from RDR)*

Section 3.6 RF power source presents the common components of the RF system for the KCS and DKS systems, i.e. the 120 kV Marx Modulators and the 10 MW Multiple Beam Klystrons (MBKs) that they power. Also, the local RF distribution system that divides up the feed power to the cavities in the tunnel is described.

Section 3.7 Low-level RF control concept covers the design and operational aspects of the low level RF (LLRF) system which are required to stabilise the vector sum of cavity voltages to within less than 1% across the beam pulse. This includes the more 'global' control via closed-loop feedback on the klystrons, as well as local (per cavity) compensation of Lorentz force frequency detuning using piezo-electric controllers.

Chapter **??** and Chapter **??** present details of the site-dependent variants – including cryo segmentation, RF power distribution and details of the LLRF controls systems — for the flat and moutain topographies respectively.

3.2 Cavity production specifications

3.2.1 Cavity Design

Figure 3.4 shows schematics of a baseline 9-cell superconducting cavity and the assembly with liquid helium (LHe) tank. Table 3.6 summarizes main design parameters of the cavity.

Table 3.6. Cavity parameters for the ML SCRF cavities.

Parameter	Value
Type of accelerating structure	Standing wave
Accelerating mode	TM_{010}, π mode
Type of cavity-cell shape	Tesla (or Tesla-like)
Fundamental frequency	1.300 GHz
Gradient averaged in operation (spread allowed)	31.5 MV/m ($\pm$20%)
Quality factor averaged in operation	$\geq 1 \times 10^{10}$
Gradient averaged in qualification (spread allowed)	35.0 MV/m ($\pm$20%)
Quality factor averaged in qualification	$\geq 0.8 \times 10^{10}$
Active length	1038.5 mm
Total length (beam flanges, face-to-face)	1247.4 mm
Input-coupler pitch distance, including inter-connection	1326.7 mm
Number of cells	9
Cell to cell coupling	1.87%
Iris inner diameter	70 mm
Equator inner diameter	$\sim$210 mm
R/Q	1036 Ω
Geometry factor	270 Ω
E_{peak}/E_{acc}	2.0
B_{peak}/E_{acc}	4.26 mT/(MV/m)
Tunable range	$\pm$300 kHz/mm
$\Delta f/\Delta L$	315 kHz/mm
Number of HOM couplers	2
Q_{ext} for high impedance HOM	$< 1.0 \times 10^5$
Material:	
- 9-cell cavity, HOM coupler, and beam-pipe	Nb (RRR $\geq 300, \sigma_{0.2} \geq 39$ MPa)
- LHe tank	Ti-Alloy
Max design pressure (high-pressure safety code)	0.2 MPa
Max hydraulic-test pressure	0.5 MPa

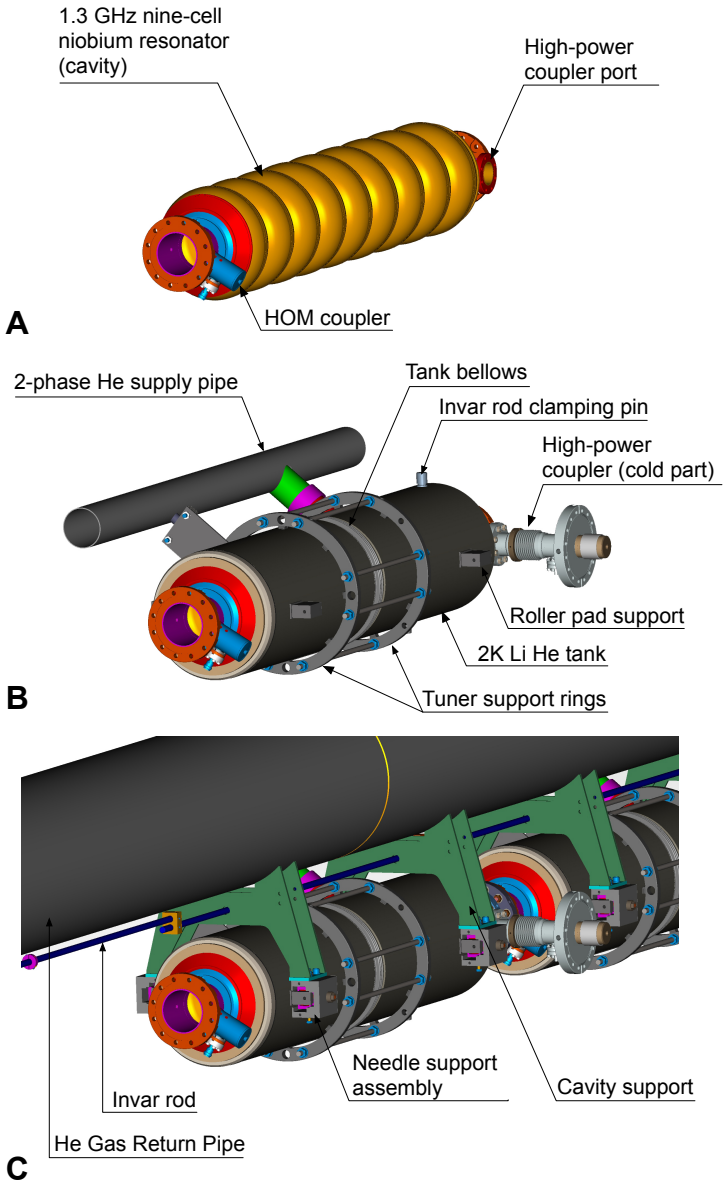

Figure 3.4. The baseline cavity package and string assembly: (A) the nine cell cavity (resonator); (B) the "dressed" cavity, showing the helium tank, 2-phase helium supply, high-power coupler (cold part) and the mount for the cavity tuner; (C) cavity package mounted into the cavity string and cryomodule. (Note the "blade" cavity tuner is not shown.) (**Ed:** *NJW: Do not have a CAD model showing the blade tuner unfortunately.)*

3.2.2 Cavity fabrication and surface processing

The fabrication process of ILC superconducting cavities and their surface treatment have substantially matured during the Technical Design Phase. The R&D leading to these procedures — as well as a more detailed discussion of the steps involved — can be found in Part I Section **??**. The procedure is briefly summarised below:

- 9-cell cavity fabrication:
  - Preparation of raw material (niobium sheet metal) with inspection
  - Components fabrication (using press, machining and electron beam welding (EBW))
  - Assembly of 9-cell cavity (using EBW)
  - Inner-surface inspection (optical inspection)
- Cavity surface treatment:
  - Light etching with buffered chemical polishing (BCP) (10 µm)
  - Heavy electro-polishing (EP) (100∼120 µm)
  - Post-heavy-EP cleaning
  - Out-gassing in vacuum furnace (800°C for 2 hours)
  - RF tuning with non-contacting bead-pull method
  - Light-EP (25 µm)
  - Post-light-EP cleaning
  - First high-pressure water rinsing (HPR) 3 passes (∼6 hours)
  - First clean room assembly
  - Final HPR 3 passes
  - Final assembly in clean room
  - Leak check
  - In-situ baking at 120°C for 48 hours
- Assembly of LHe tank:
  - Pre-assembly check-out of tank components. Validation of their hermeticity and mechanical sturdiness under over-pressurized conditions from the standpoint of safety.
  - Assembly of LHe tank with the main 9-cell cavity part
  - Inspection of leak-tightness, as required by high-pressure gas safety rules
- Testing of completed cavity in a vertical test stand, and possible 2nd cycle:
  - Cool-down,
  - RRR measurement
  - Q vs gradient measurement with π-mode and pass-band mode test

– Tuner functioning and LLRF control response

There are two key issues concerning the mechanical fabrication of the cavities for the ILC. The first is the quality assurance of the niobium materials. The second is the process quality control of electron beam welding. The sheet and bulk niobium which are supplied by vendors must be scanned for detecting and avoiding materials with defects, and once accepted, they have to be the protected from mechanical damages and dust throughout the manufacturing process. Defective materials can become a source of ultimate performance limitation of a completed cavity. Impurities which are introduced in the welds and in the heat-affected zones next to welds will also limit the gradient performance. Weld joints must have smooth beads without surface irregularities and without sharp edges on locations where the weld puddle meets the bulk material. A defect on the equator weld will in general result in a local enhancement of the magnetic field, and a single such defect can be the cause a thermal quench, leading to a degradation of field gradient performance. (**Ed:** *NJW: NKT required 'qualification' of this, but as I'm sure he knows that is impossible. I have slightly modified the text.)* Current production experience suggests some 10–20% of cavities (**Ed:** *NJW: correct number?)* produced could suffer from this problem. Therefore procedures for repairing the cavity surface has been developed (see Part 1 Section **??** (**Ed:** *NJW: check if this is the right reference)*).

The surface preparation steps have developed over many years into the established recipe outlined above. The details can be found in Part 1 Section **??**. In summary, the process steps are designed to:

1. remove material damage incurred during the fabrication process or handling by using chemical procedures;

2. remove the chemical residues left over from the material removal steps;

3. remove hydrogen in the bulk niobium which has been captured during the chemical procedures in step 1;

4. remove any particulate contamination which entered during the cleaning and assembly steps; and

5. close up the cavity to form a hermetically sealed structure.

Fig. 3.5 provides an overview of the cavity production process, and in particular the approach to testing. A key issue for mass production is achieving the required performance yield ($> 90\%$) in a cost-effective manner. The current approach — based on existing R&D experience discussed in Part I Section **??** — is to allow specific steps to be iterated in the production process. The first test in this respect is an optical inspection (Part I Section **??**) of the cavity directly after fabrication, but before any surface treatment. This inspection is intended to identify candidates surface defects as described above, which would limit the cavity performance to below 20 MV/m. These cavities (an estimated 20% of the total) would be removed from the production line and mechanically repaired using the techniques described in Part I Section **??**. A second optical inspection is made after initial surface treatment

(bulk electro-polishing, 800° heat treatment, followed by mechanical RF tuning), to identify weld defects that may have been uncovered by the removal of 150 µm niobium during bulk electro-polishing (approximately 4% of the total). The cavities then undergo the final surface preparation steps and the RF antenna, two HOM couplers and the helium tank are mounted. The final performance (acceptance) test is a low-powered RF test in a vertical cryostat at 2 K (so-called vertical test), where the cavity ultimate performance is measured (maximum acceptable gradient, quality factor, field emission etc.)[1]. Again based on the current status of the R&D, It is expected that some fraction of cavities (∼20%) will require an additional application of the fine EP surface treatment (a so-called "second pass"). These cavities will need to have their HOM couplers and RF antennas removed, but unlike the first pass, the fine EP will be performed with the helium tank in place. After re-processing, the cavity is again reassembled with the antenna and HOM couplers, and a second vertical test is performed. Although a third-pass is feasible, it is not considered necessary and is not included in the cost estimate for the cavity mass production.

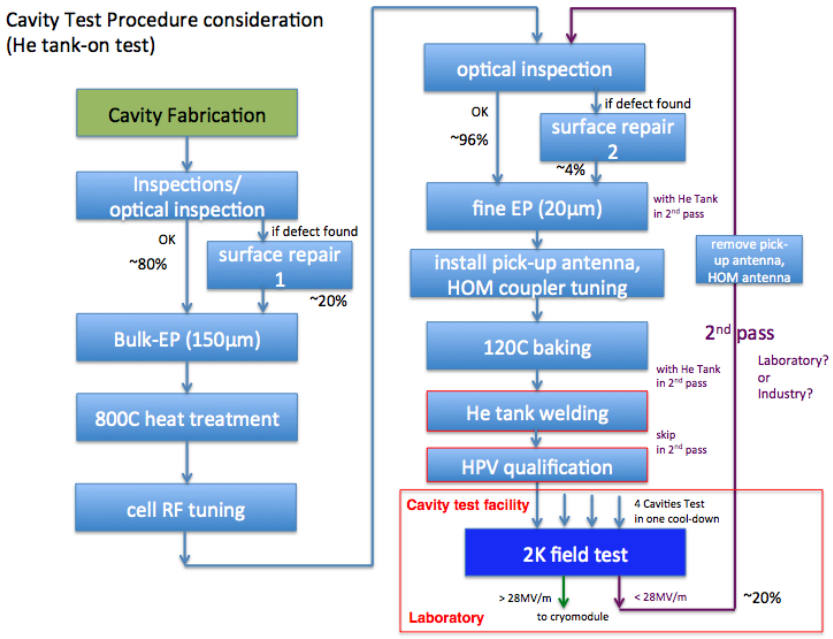

Figure 3.5. Flow chart of the cavity treatment and test. [Fig. 3.5, right now is not explicit about where the cavity tuning happens. I think it should be right after fine EP and before installation of pick-up antenna, and it has to be mentioned. All EPs come together with HPWR, I think, but neither this figure nor the main text are much explicit about it. They should be.]

The performance of the cavity vertical test performance and the choice of remediation steps needed in the event of failures are discussed in Part I Section **??**.

[1]The decision to assemble the tank and HOM couplers before the vertical test is driven by mass production considerations, and follows the same approach taken for the cavity production for the European XFEL project.

It is expected that the mechanical fabrication and surface preparation will be performed by industry. However, the final RF test will be performed by a collaborating laboratory or institute, which will host the required cryogenic and RF test infrastructure and personnel. The second-pass process steps could alternatively be dealt with in the lab's infrastructure (as is the case for the European XFEL), or returned to industry.

3.3 Cavity integration

The most important part of the cryomodule is the cavity package, which is an integrated system consisting of a 9-cell cavity, contained within a titanium helium jacket connected to a helium supply pipe, a fundamental-mode power coupler, a frequency tuner, and a magnetic shield (See Fig. 3.4 A and B). The design of the ILC cavity system is based on the original TESLA design used in TTF/FLASH and currently being produced for the European XFEL project. The ILC cavity package consists of the following:

- a nine-cell niobium resonator (cavity), complete with two HOM couplers and RF antenna, flanges etc;
- a titanium helium tank (cryostat), split with a bellows to support the mechanical tuner;
- the mechanical tuner itself (so-called blade tuner), mounted on the two halves of the helium tank;
- a high-power fundamental-mode RF coupler;
- a magnetic shield which surrounds the cavity and is installed inside of the helium tank.

The cavity and its manufacture are discussed in the previous section (Section 3.2). The remainder of this section will describe the baseline high-power coupler, frequency tuner, helium tank and HOM couplers.

3.3.1 Fundamental-mode power coupler

The 'TTF-III' input coupler was originally developed for TESLA [22][21], and has since been modified by a collaboration of LAL and DESY for use in the European XFEL [19]. Due to the maturity of the design and extensive experience with this coupler, it has been adopted as the baseline design of the fundamental power coupler for the ILC. The main specifications of this input coupler are listed in Table 3.7.

The coupler is a complex device containing some 130 parts. As with the cavities, the couplers must be assembled in very clean environments.

3.3.1.1 Mechanical design

A 3-dimensional sectioned schematic of the coupler assembly is shown in Fig. 3.6. The coupler is separated into a warm and cold part as shown, the latter of which is mounted into the cavity at 2 K. RF power is brought in via a rectangular waveguide (WR650) into the "door-knob" mode converter on the left end at room temperature (warm transition). The RF power then propagates through a coaxial transmission line into the cavity beam pipe via the antenna (at 2 K). Both the warm and cold parts have a ceramic RF window, which protect and separate the cavity vacuum and the vacuum inside the warm coupler part. (The cold part shares the same

Table 3.7. Main specifications of the input coupler.

Parameter	Specifications
Frequency	1.3 GHz
Operation pulse width	1.6 ms
Operation repetition rate	5 Hz
Maximum beam current	9 mA
Accelerating gradient of cavity	31.5 MV/m (average)
Required RF power in operation	$>$ 400 kW for 1.6ms pulse duration
Range of external Q value	$(1.0 \sim 10.0) \times 10^6$ (tunable)
RF process in cryomodule	$>$ 1200 kW for $\leq$ 400 μs pulse width
	$>$ 500 kW for $>$ 400 μs pulse width
RF process with reflection mode	$>$ 600 kW for 1.6 ms pulse width
	in test stand.
RF process time	$<$ 50 hours in warm state
	$<$ 20 hours in cold state
Heat load of coupler	$<$ 0.063 mW (2K static)
	$<$ 0.171 W (5K static)
	$<$ 1.70 W (40K static)
	$<$ 0.018 W (2K dynamic)
	$<$ 0.152 W (5K dynamic)
	$<$ 6.93 W (40K dynamic)
Number of windows	2
Bias viltage capability	Required
Instrumentation	Vacuum level: $\geq$ 1
	Spark detection: 0
	Electron detection: $\geq$ 1 at coaxial part
	Temperature sensor: $\geq$ 1 at window

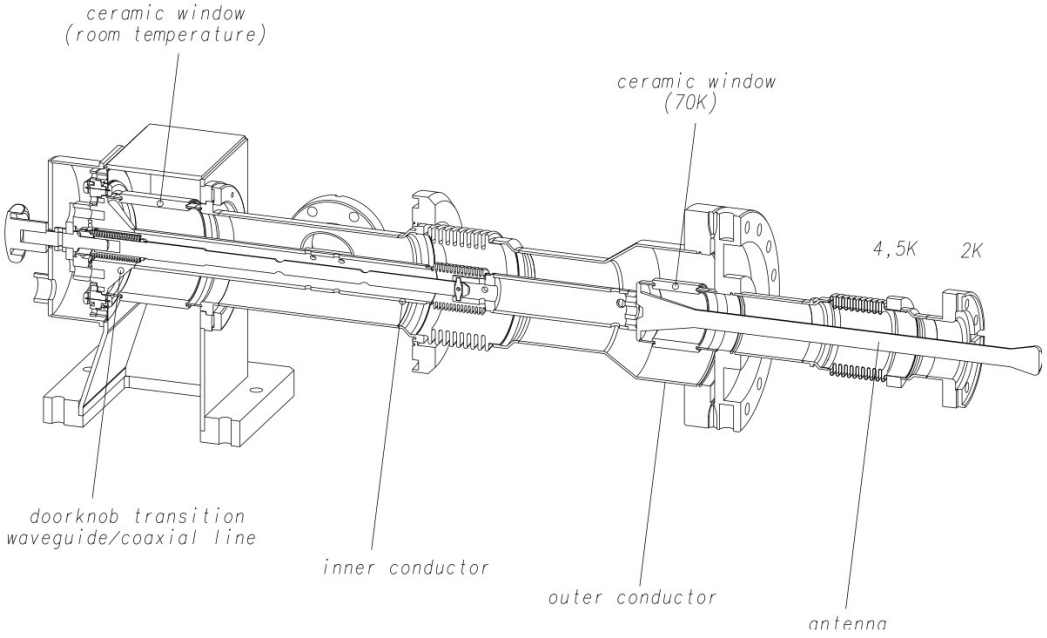

Figure 3.6. Schematic drawing of TTF-III input coupler.

vacuum with the cavity.) Both RF windows are cylindrical ceramic pieces made of Al_2O_3, the vacuum surfaces of which are coated with a few nanometers thickness of titanium-nitride in order to prevent multipacting. The two bellows (warm and cold) in the outer conductor allow a ±10 mm adjustment of the antenna penetration into the cavity beam pipe to change the coupling to the cavity, providing a range of Q_{ext} of 1–10 × 10^6. The antenna position (Q_{ext}) is adjusted via a tuning rod housed in the central conductor, and driven by a remote actuate at the end of the warm transition.

The outer conductor is made of thin SUS whose inner surface has a 10 µm thin copper plaiting. The tight tolerance on the copper plaiting is driven by a balance between (i) providing enough electrical skin depth to prevent penetration of the RF into the SUS, thus minimising ohmic losses, and (ii) achieving a thermal balance between heat conduction from the warm end of the coupler (static load) while providing cooling for the RF losses (dynamic load).

Each input coupler is equipped with three electron current pick-up probes for monitoring discharges inside the coupler. A provision is made to DC-bias the inner conductor to suppress the onset of multipacting. The warm coupler vacuum is maintained by a separate vacuum pumping system at a pressure of XXX torr.

3.3.1.2 Initial coupler processing (acceptance testing) and final assembly

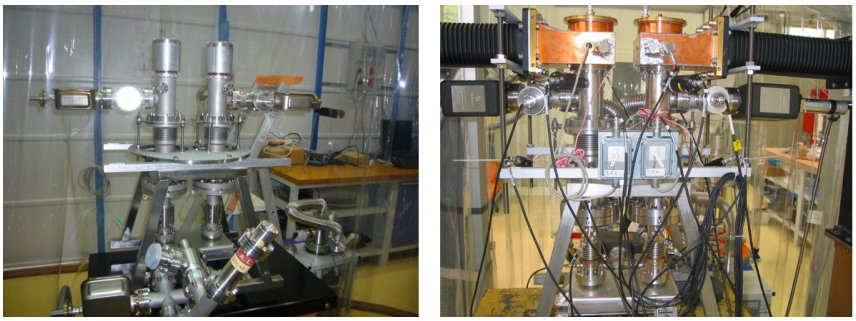

Figure 3.7. Set-up of high power test stand at LAL for the European XFEL.

After receipt from industry and before assembly into the cavity, the input couplers undergo warm RF-conditioning, which also forms part of the coupler acceptance testing. Coupler test facilities will likely be located at collaborating institutes, such as the one for the European XFEL at LAL, Orsay. The coupler test facility requires clean room facilities for the handling and cleaning the coupler parts, pumping and baking systems, and high-power RF systems for processing of the couplers. Fig. 3.7 shows the set-up for warm coupler conditioning at LAL, where pairs of coupler are conditioned together.

The current accepted process, including clean room assembly of the parts and subsequent cleaning and in-situ bake-out, are the result of extensive R&D at LAL for the European XFEL [20], which has resulted in a significant reduction in the time required to fully condition the couplers (now approximately 20 hours). Fig. 3.8 shows the steps in preparing the coupler for the warm RF processing. First, the

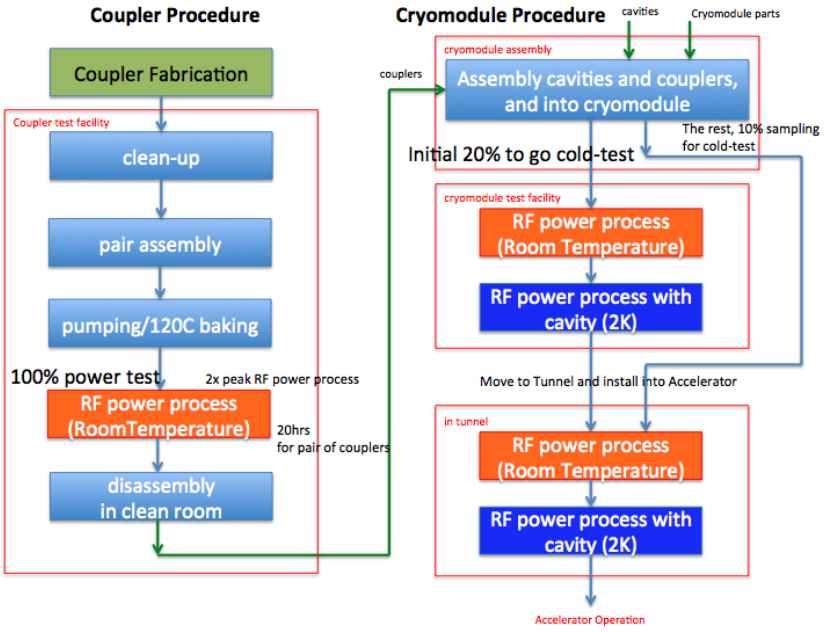

Figure 3.8. Flow chart of the input coupler process and test. (**Ed:** *NJW: modify figure to only include LHS.)*

interior of coaxial parts and window ceramics of both the warm and cold parts of the couplers are inspected and cleaned in a clean-room environment, after which they are assembled together. A pair of couplers are then installed in a special rectangular waveguide system for RF processing. The typical conditioning procedure is to raise the RF power and pulse width in steps from near zero to predetermined maximums, avoiding out-gassing in excess of a prescribed vacuum trip level ($\sim 2 \times 10^{-7}$ mbar). The RF pulse width starts from 20 µs, and then increased to 50, 100, 200, 400, 800, 1300, and 1500 µs. The entire procedure is automated

Once successfully processed, the couplers are disassembled in a clean room to avoid any contamination of their interior surfaces, and then sealed and transported to a cryomodule assembly facility. Here, the cold and warm parts are separated and the cold part of the coupler mounted into the cavity in a class-10 clean room during the cavity string assembly. The warm coupler part is installed only after the complete string and cold mass have been installed into the cryomodule vacuum vessel. Final assembly of the warm couple part is made in a clean environment provided by mobile clean-room cabins.

After installation of the complete coupler into the cryomodule, further light conditioning is required at both room temperature and 2 K. This processing is performed either as part of the cryomodule tests, or in-situ after installation in the accelerator tunnel (see Section **??**).

3.3.2 Frequency tuner

The mechanical cavity tuner is required to provide two functions:

- a slow mechanically adjustment the frequency of the cavity and bring it on resonance (static tuning);
- a fast 'pulsed' adjustment using a piezo system to dynamically compensate Lorentz force detuning during the RF pulse.

Specifications for the frequency tuner system is summarised in Table 3.8. The "Blade Tuner" design [14, 13, 12, 11], which has been developed by INFN Milano-LASA as a coaxial and light tuning solution for TESLA-type cavities, has been adopted for the ILC baseline.

Table 3.8. Main specifications of the frequency tuner.

Tuner	Parameter	Specifications
Slow tuner		
	Tuning range	> 600 kHz
	Hysteresis	$< 10\mu$m
	Motor characteristics	Step motor, power-off holding, magnetically shielded
	Motor location	Inside 5K shield, accessible from outside
	Magnetic shield	< 20mG
	Heat load by motor	< 50 mW at 2K
	Motor lifetime	$> 20 \times 10^6$ steps
Fast tuner		
	Tuning range	>1KHz at 2K
	LFD residuals	< 50 Hz at 31.5 MV/m flat-top
	Actuator	Piezo actuator, located inside 5K shield, Two actuators for redundancy
	Heat load by actuator	< 50 mW at 2K
	Magnetic shield	< 20mG
	Actuator lifetime	$> 10^{10}$ pulses

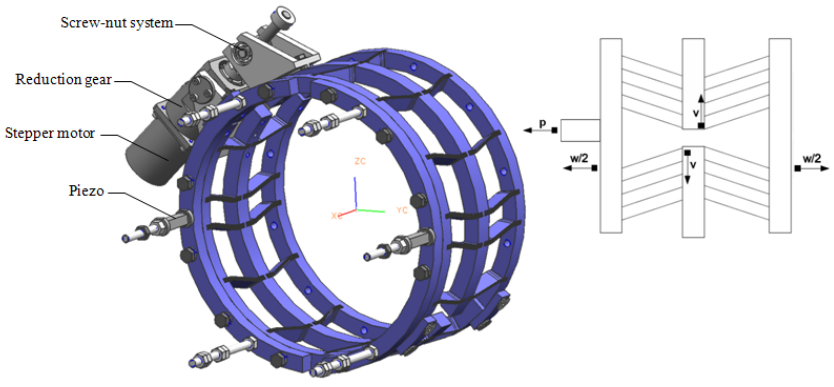

Figure 3.9. Blade Tuner graphic view and its cinematic. [Explain what the arrows mean as they are indicated as p, $w2$, and v]

Fig. 3.9 shows the tuner. The azimuthal movement of the central ring is converted into the required longitudinal cavity strain without backlash via the elastic blades. The tuner mechanics as well as the blades are made of titanium, which provides both

mechanical strength and a small thermal expansion coefficient. The slow tuning action is generated by a stepper motor operating at 5 K, coupled via a mechanical reduction gear, to rotate a threaded shaft which azimuthally moves the central ring. [NOTE: Please, check if this is correct.] A CuBe threaded shaft is used as a screw-nut system. Fast tuning action is driven by two piezoelectric ceramic actuators mounted symmetrically on either side of the cavity as shown in Fig. 3.9, which efficiently allows the transfer of their stroke to the helium tank, in series with the slow mechanical tuner. The coaxial tuner is installed on a mid location of the helium tank that is split in two halves by a bellow. This arrangement allows for simplification of end cone regions of the cavity which need to accommodate fundamental mode and HOM couplers.

The blade-tuner and in particular the piezo actuators need to be under compression to operate. This is achieved by applying an initial pre-load using a calibrated cavity tensioning, which provides an initial frequency de-tuning and the correct amount of compression for the tuner.

The tuner mechanics, motor, gearbox and piezo actuators must be designed for high-reliability, since a failure of the tuner mechanism will seriously hinder the optimal operation of that cavity, and in general these devices are not accessible once installed into the cryomodule. Possible solutions which could allow limited access to (for example) the motor and gearbox are being considered, but require much more detailed investigation of the impact on the cryomodule design, and in particular the heat loads. These studies are on going.

3.3.3 HOM couplers

(**Ed:** *NT 20120901 - Created a place holder for this stuff which is completely missing now.)*

3.3.4 Helium jacket and its interface

3.3.4.1 Helium jacket

The helium tank design for the ILC cavity package consists of a cylindrical jacket connected to a 2-phase helium supply pipe, both of which are constructed from titanium (see Fig. 3.4 B).

Each helium jacket has two pairs of "roller pad supports" made of titanium and welded at the horizontal mid-plane of the tank. The supports are used to hang the cavity from the cavity support arms which extend underneath the gas return pipe (Fig. 3.4 C). The tank also has a clamping pin to connect it to the invar rod that runs the entire length of the cryomodule. The clamp (and the invar rod) prevents the cavities from moving longitudinally during cool-down and warm-up, keeping the locations of the high-power couplers fixed. The roller pad supports are mounted in slide bearings and adjuster bolts (needle support assembly), which allows the for the contraction and expansion of the helium gas return pipe, to which the cavity support arms are fixed.

The helium tank has to accommodate the tuner system as discussed in Section 3.3.2. For this purpose the tank has a thin titanium cylindrical bellows located

at its centre. On both sides of the bellows, two flanges are welded for installation of the blade tuner.

The 2-phase helium pipe has a short branch made of another pipe with the same diameter and this branch is welded to an adaptor hole provided on the helium tank. The 2-phase helium pipes of neighbouring cavities have their lengths chosen such that they can be readily welded to each other via bellows when they are assembled into a cryomodule.

3.3.4.2 Magnetic shield

The superconducting cavities have to be shielded from external magnetic fields to achieve their maximum performance. A conceptual drawings of the magnetic shield installation is shown in Fig. 3.10. The magnetic shields are a cylindrical shape and are incorporated inside the titanium helium tank, together with additional conical shield pieces used between the end plates and end cavity cell walls. Incorporating the shields with the helium tank eliminates the need to install more complex external magnetic shields around the blade tuners. The string assembly procedure is also simplified, although at the expensive of a more complicated cavity production.

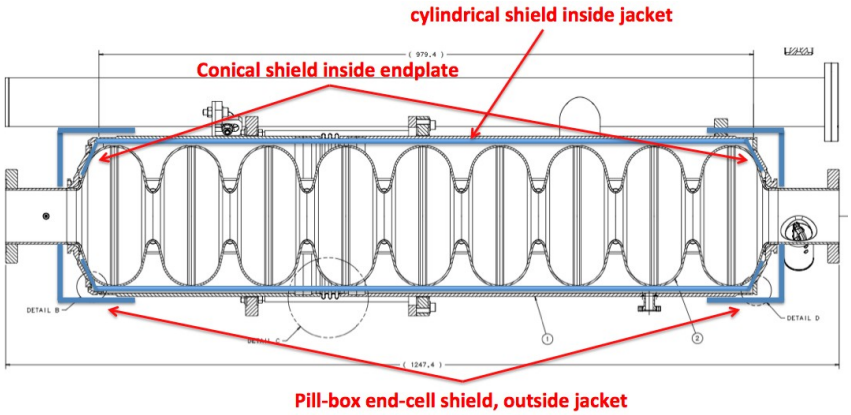

Figure 3.10. Sketch showing the location of the magnetic shields placed inside the helium tank.

The conical shields used near the endplates are made of two halves which are slid into the space between the end cells of the cavity and the end plates. After insertion, the two halves are bolted together. The remaining part of the shield to cover the rest of the cavity is basically a cylinder of sheet metal which wraps around the cavity. The cylindrical and conical shields are overlapped at both ends of the cylinder, as shown in Fig. 3.11. To reduce the field leakage from the open aperture of both beam pipes, additional magnetic shields in the form of a half pill-box are placed outside of the helium tank, as shown in Fig. 3.10.

3.3.4.3 Flanges and seals

All the cavity flanges are made of Nb-Ti alloy and use a hexagonal ring seel made of aluminium alloy (Al-Mg-Si) for vacuum sealing. Flanges are required for the two

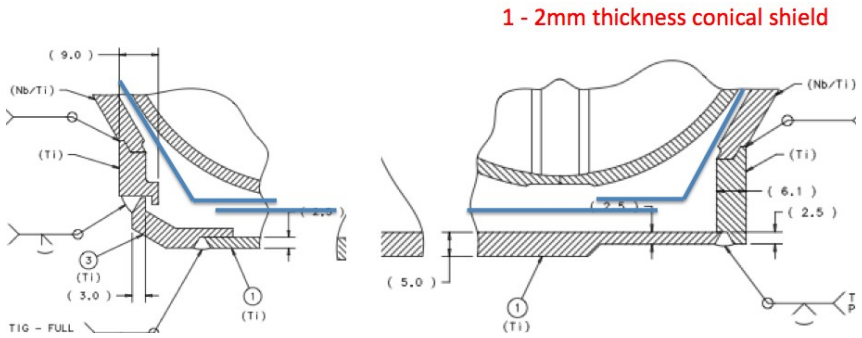

Figure 3.11. Sketch showing the overlap of the cylindrical and conical shields at the ends of the cavity.

beam pipes, input coupler port, fundamental power pick-up port, and two HOM pick-up ports. The surfaces of the flanges which meet the seal should be machined and polished to a very smooth surface finish. The edges of the hexagonal seal which meet the flange surface need to be sharp and firm.

3.3.5 Plug-compatible design

(**Ed:** *NJW: IMO this introductory text is out of place here, and really belongs in Part I and possible even in the PIP)* .

The GDE introduced the concept of plug-compatibility during the Technical Design Phase in recognition of the fact that certain parallel efforts in the world need to be accommodated while pursuing a forward-looking design development of critical components required at the ILC. For this purpose the GDE developed a set of interface definitions for the cryomodule and its associated sub-systems. These interface definitions would in principle allow components of different internal designs be co-assembled in a same cryomodule. During the R&D phase, plug compatibility supported parallel development of technologies such as cavities, tuners, and high-power couplers. It also allowed each of the regional teams to develop in-house design expertise, and to encourage pursuit of local innovation, while guaranteeing that outcomes of such efforts will be always useful and usable globally.

The concept can equally be extended to mass production models for construction of the project, where plug-compatibility will:

- support competition between multiple suppliers, inducing cost reduction, while allowing variants within a common design envelope;
- allow for multiple (in-kind) contributors, each of which may arrive at a different cost-optimised design, therefore maximising the benefit of the local industrial capability and experience;
- encourage intellectual interest from each contributor to promote regional, national or institutional centres for integration and test of the cryomodule or any of its subcomponent packages.

The performance of the plug-compatible components consider so far must adhere to the specifications which are given in this chapter; specifically: the cavity (Section 3.2); fundamental-mode coupler (Section 3.3.1); mechanical tuner and helium tank (Section 3.3.2 and Section 3.3.4 respectively). In addition, the physical envelope of the the components and their interface definitions must also be uniquely specified, and these are given below.

3.3.5.1 Mechanical interface definitions

3.3.5.1.1 Cavity resonator The boundary and the interfaces for the cavity are defined as shown in Fig. 3.12. The length of a cavity as measured from the surface of the two beam port flanges is 1247 mm. DN78 flanges are used for the two beam pipe ports and a DN40 flange is used for the input coupler.

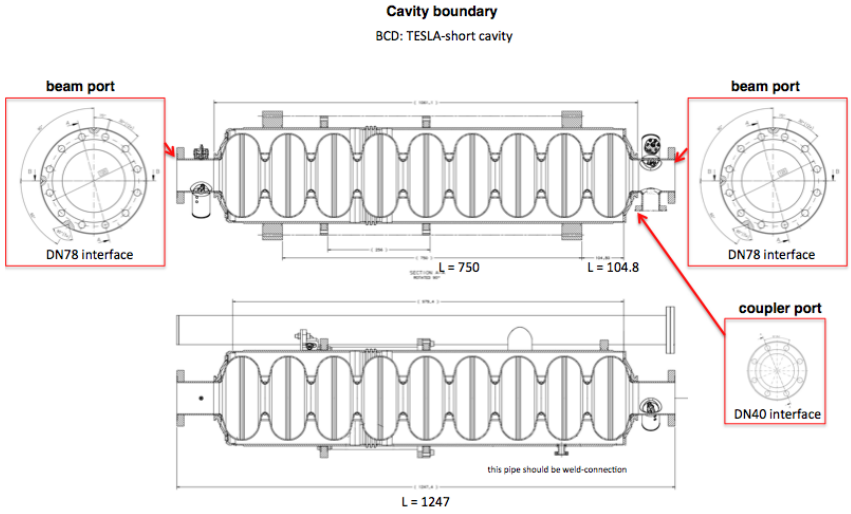

Figure 3.12. Interface definition of the cavity.

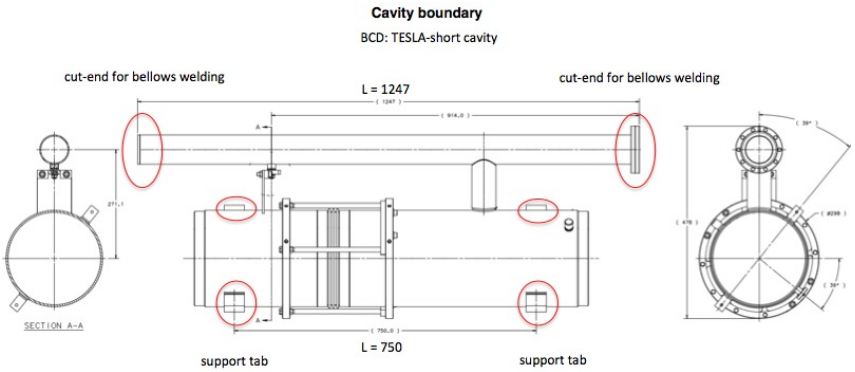

Figure 3.13. Interface definition of the helium jacket.

3.3.5.1.2 Helium tank The interfaces of the helium tank are defined by the four roller pad supports and two ends of the 2-phase helium supply pipe as shown in Fig. 3.13. The end finish of the 2-phase helium supply pipe has to have a weld-ready finish for connection of the titanium bellows. The roller pad supports have to have smooth surfaces, compatible with the needle support assembly.

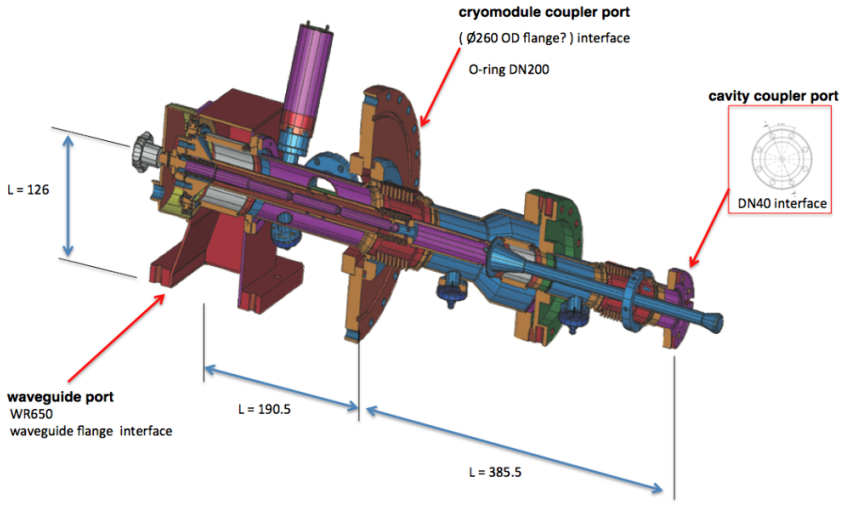

Figure 3.14. Interface definition of the input coupler.

3.3.5.1.3 Fundamental-mode input coupler The interfaces of the input coupler are defined by the cavity coupler port, cryomodule coupler port and the rectangular waveguide port, as shown in Fig. 3.14. The cavity coupler port is a DN40 interface flange which uses aluminium-made hexagonal sealing. The cryomodule coupler port is a flange with an outer diameter of 260 mm which uses a DN200 O-ring seal.

3.4 Cryomodule design including quadrupole and cryogenic systems

3.4.1 Overview

Cryomodules are the modular building blocks of the ILC superconducting main linacs, and need to fulfil the following main functions:

1. provide mechanical support for beamline elements as cavities and focussing elements;
2. facilitate achievement of the necessary alignment tolerance and stability according to beam dynamics specifications;
3. create and maintain in an efficient way the cold environment needed for the cavity and magnet operation.

The cryomodules represent the major heat loads at LHe temperatures, and therefore play an important role in the overall cryogenic system optimisation.

The highly-integrated design concept for the cryogenic systems leading to a high filling-factor and reduced overall cost has been introduced in Section 3.1. In particular the concept of the use of single large cryoplants to cool kilometre-long *cryo-units* (similar to the LHC). Shorter segmentation *cryo-strings* are required to achieve segmentation of the insulating vacuum and of the two-phase helium line.

Each of the 12.652 m long cryomodules contains either nine cavities (Type A), or eight cavities and one superconducting quadrupole package (including horizontal and vertical dipole correctors and a BPM) located at the centre of the cryomodule (Type B). The cavities and quadrupole package are integrated into the cryomodules along with their supporting structures, thermal shields and insulation, and all of the associated cryogenic piping required for the coolant flow distribution along a cryogenic unit without the need for additional external cryogenic distribution lines.

All the 14,742 1.3 GHz cavities in the ILC main linacs grouped into 1,701 cryomodules. (1,134 Type A, and 567 Type B). Another 152 cryomodules are located in the e^+ and e^- sources and RTML bunch compressors. Most of these are either the standard Type A or Type B cryomodules, although the sources contain a few with special configurations of cavities and quadrupoles.

3.4.2 Cryomodule technical description

Fig. 3.15 shows a longitudinal sectioned view of the Type-IV cryomodule (Type B). The design is a modification of the type developed and used in the TESLA Test Facility (TTF) at DESY, with three separate vacuum envelopes (beam vacuum, isolation vacuum and power coupler vacuum) [29]. The cavity spacing within the cryomodule is $(6 - 1/4)\lambda_0 = 1.327\,\mathrm{m}$.

The quadrupole package will use the conduction-cooled split quadrupole described in Part I Section **??**.

Flanged bellows are located between beamline components. RF- and HOM-couplers lines are connected to the cavity beam tubes. Manually operated valves

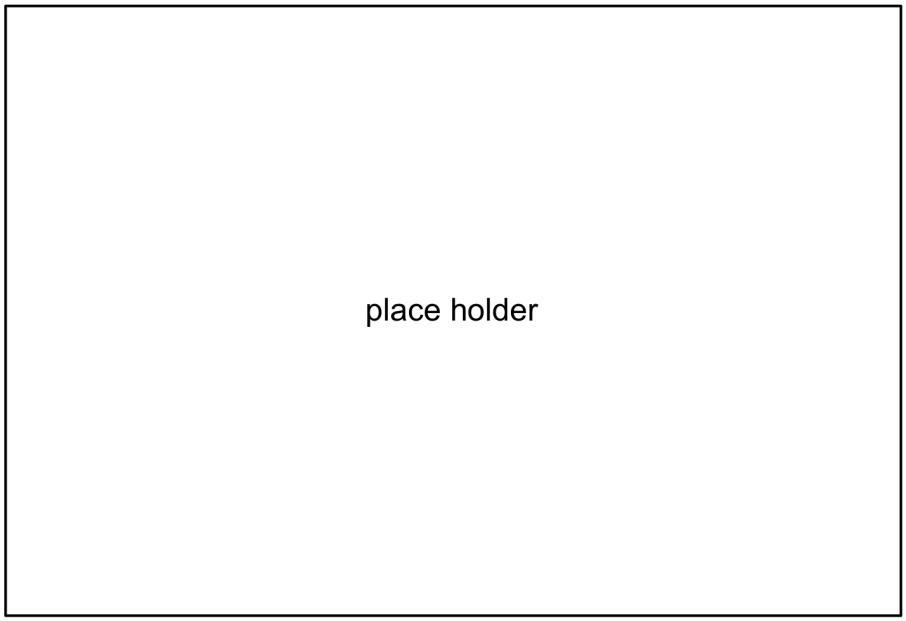

Figure 3.15. Longitudinal View of a Cryomodule

required by the clean-room assembly terminate the beam pipe at both module ends. The valves are fitted with simple RF shields.

The decision to place the quadrupole package in the middle of the cryomodule (as in the Type IV design) allows to define a standard interconnection interface for all main linac cryomodules, irrespective of their sub-type, streamlining the tunnel assembly procedures for module connections.

3.4.2.1 The Cryomodule Cross Section

Figure 3.16 shows a cross-section of a the Type IV ILC Cryomodule derived from the TTF-III design [1, 2]. The largest component of the transverse cross section is the 300 mm diameter helium gas return pipe (GRP) which acts as the structural backbone for supporting the string of beamline elements and allows recovery of the mass flow of He vapors at a negligible pressure drop along the cryostrings, to preserve temperature stability.

The GRP is supported from the top by three composite posts with small thermal conduction from the room temperature environment. The posts are connected to adjustable suspension brackets resting on large flanges placed on the upper part of the vacuum vessel. This suspension scheme allows to correctly align the axis of the cavities and quadrupole magnets independently from the flange position, without the requiring expensive precision machining on these vacuum vessel components. The center post is fixed to the vacuum vessel, while the two remaining posts are laterally adjustable and can slide on the flanges to allow the GRP longitudinal contraction/expansion with respect to the vacuum vessel during thermal cycling. Each post consists of a fiberglass pipe terminated by two shrink-fit stainless steel flanges. Two additional shrink-fit aluminum flanges are provided to allow intermediate heat

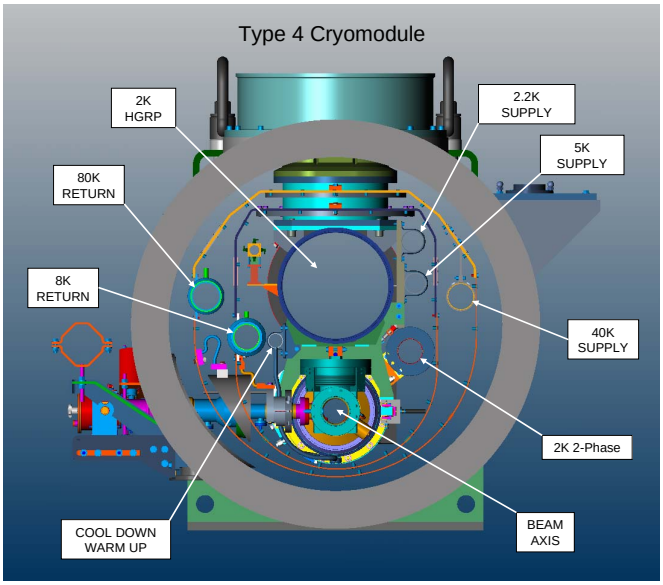

Figure 3.16. Representative Cryomodule Cross-Section and longitudinal view. (**Ed:** *What does "HGRP" stand for? Perhaps you should relabel it simply as "GRP" to make it consistent with the text.)* (**Author:** *Will provide updated x-y and x-z sections, with new labels.)*

flow intercept connections to the 5–8 K and 40–80 K thermal shields; the exact location of these flanges has been optimized to minimize the heat leakage [3].

3.4.2.2 Transverse / longitudinal cavity positioning and alignment

The cavities are supported from the GRP by means of stainless steel brackets holding the four titanium roller pads on their helium jacket via a longitudinal sliding mechanism, which provides also adjusting screws and pushers for alignment in the transverse (vertical-horizontal) planes. A mechanical, coaxial (blade) and a piezoelectric tuner are mounted on the cavity jackets.

During cool down the two ends of the ∼12 m long gas return pipe move by up to 18 mm toward the center of the module. The cavity sliding support allows the cavity position to be completely decouple from the large GRP contraction induced by the cooldown, and avoids large stresses acting on the cavities due to differential shrinkage. To maintain the longitudinal position of the cavity coupler flange within 1 mm from the coupler port on the warm vacuum vessel—in order to limit large coupler movements occurring with differential contraction—each cavity is clamped to a long invar rod, which is in turn longitudinally anchored at the neutral fixed point of the GRP at the center post.

The beam pipe interconnection between the cryomodules consists of a 0.38 m long section between the end valves that incorporates a Higher Order Mode (HOM) absorber, a bellows, and a vacuum pumping port; the latter connected to a flange

in the vacuum vessel every ninth cryomodule.

3.4.2.3 Thermal Radiation Shields

The cryostat includes two aluminum thermal radiation shields operating in the temperature range of 5–8 K and 40–80 K, respectively [4]. The use of a double thermal radiation shielding allows to reduce the radiative thermal load at 2 K to a negligible amount. Each shield is constructed from a stiff upper part, and multiple lower sections (according to the number of the cold active components, e.g., cavities, magnets). The upper part is supported by the intermediate flanges on the fiberglass posts; constrained at the center post but sliding on the two lateral posts, to which they are still thermally connected. The 'finger–welding' technique [4] is used both to connect each thermal shield to its properly shaped aluminum cooling pipe, and the lower shield parts to the upper ones, by providing good thermal conduction without inducing high stresses on the structure.

Blankets of multi-layer insulation (MLI) are placed on the outside of the 5–8 K and the 40–80 K shields. The 5–8 K shield blanket is made of 10 layers of doubly aluminized mylar separated by an insulating spacer while the 40–80 K blanket contains 30 layers. In addition, helium jackets for cavity and magnet packages, gas return pipe and 5–8 K pipes are wrapped with 5 layers of MLI as a mitigating provision to reduce heat transfer in the event of a vacuum failure.

3.4.2.4 The Vacuum Vessel

The cryostat outer vacuum vessel is constructed from carbon steel and has a standard outer diameter of 38″. Adjacent vacuum vessels are connected to each other by means of a flanged cylindrical sleeve with a bellows. Adjacent vessels have a flange-to-flange distance of 0.85 m, allowing sufficient space for performing the cryogenic connections between modules by means of automated orbital welders. In the event of accidental spills of liquid helium from the cavity vessels, a relief valve on the main vessel body together with venting holes on the shields prevent excessive pressure build-up in the vacuum vessel. Wires and cables of each module are extracted from the module using metallic sealed flanges with vacuum tight connectors. The insulating vacuum system is pumped during normal operation by permanent pump stations located at appropriate intervals. Additional pumping ports are available for movable pump stations, which are used for initial pump down, and in the event of a helium leak. The RF power coupler needs an additional vacuum system on its room temperature side; this is provided by a common pump line for all couplers in a module, which is equipped with an ion getter and a titanium sublimation pump.

3.4.2.5 Cryogenic lines in the module

The following helium lines [5] are integrated into the cryomodules, as shown in Fig. 3.16. (**Ed:** *To make the terminology consistent, all "SUPPLY"s in labels within the Fig should be replaced with"forward", or all "forward"s in the text below should be replaced with "supply". One way or the other.]*) :

- The 2 K forward line transfers pressurised single phase helium through the cryomodule to the end of the cryogenic unit.
- The titanium 2 K two-phase supply line is connected to the cavity and magnet helium tanks. It supplies the cavities and the magnet package with liquid helium and returns cold gas to the 300 mm GRP at each module interconnection.
- The 2 K GRP returns the cold gas pumped off the saturated He II baths to the refrigeration plant. It is also a key structural component of the cryomodule
- The 5–8 K forward and return lines. The 5 K forward line is used to transfer the He gas to the end of the cryogenic unit. The 5–8 K return line directly cools the 5–8 K radiation shield and, through the shield, provides the heat flow intercept for the main coupler and diagnostic cables, and the higher-order mode (HOM) absorber located in the module interconnection region.
- The 40–80 K forward and return lines. The 40 K forward line is used to transfer He gas to the cryogenic unit end and cools the high temperature superconductor (HTS) current leads for the quadrupole and correction magnets. The 40–80 K return line directly cools the 40–80 K radiation shield and the HOM absorber and, through the shield, provides an additional heat flow intercept for the main coupler and diagnostic cables.
- The warm-up/cool-down line connects to the bottom of each cavity and magnet helium tank. It is used during the cool down and warm up of the cryostat.

The helium lines connected to the cavities and the magnets withstand a maximum pressure of 3 bar; (**Ed:** *NJW: as per email with AY changed this from 4 to 3 bar - see notes below)* . all other cryogenic lines withstand a maximum pressure of 20 bar. The helium lines of adjacent modules are welded at the module interconnection regions. Transition joints (similar to those used in the HERA magnets and in TTF and XFEL) are used for the aluminum to stainless steel transition on the thermal shield cooling lines. The cryostat maintains the cavities and magnets at their operating temperature of 2 K. (**Author:** *The implication of the above description from RDR is that the MAWP for the cavity package need to be set to 4 bar. Need to check with the cavity technical description, especially according provisions for pressure vessel compliance.)* (**Ed:** *The rest of TDR2 Chap3 remains completely silent on this issue, which by itself is a problem.])* (**Author:** *Agreed, need to provide section on pressure vessel compliance)* (**Ed:** *BL: Tom Peterson has written a long report on this: [33])* (**Ed:** *AY - 20120901: This need to be fixed. Currently, our design assumption in TDR be Design pressure 0.2 MPa (2 bar) and the maximum test pressure to be 0.3 MPa for cavity, and it would need to be the same for cryomodule cryoline without valve separation.])*

3.4.2.6 Thermal design and module heat loss estimations

A low static heat load is an essential feature required of the cryostat design; the total heat load is dominated by the RF losses, and is thus principally determined

by the cavity performance (and its spread). Table 3.9 lists the heat load assumed per cryomodule at the ILC. The table reports the average values corresponding to one Main Linac unit (ML unit), i.e., three modules in a Type A – Type B – Type A configuration. The values reported here are based on the heat load of a 12-cavity cryomodule which has been calculated for TESLA TDR [1], and refinement made on the basis of further assessments and static load measurements obtained during the Technical Design Phase with the measurements at S1-Global (Part I Section **??**) and for the European XFEL prototypes. To scale to the ILC parameters, it is assumed that the gradient is 31.5 MV/m, the cavity Q_0 is 1×10^{10}, and the beam and RF parameters are those listed in Section 3.1. These values are used for the dimensioning of the two variants of the cryogenic systems for the flat and mountainous topography respectively.

Table 3.9. Average heat loads per module. All values are in watts [29]. (**Ed:** *BL: Check whether this is consistent with EDMS values)*

	2 K		5–8 K		40–80 K	
	Static	Dynamic	Static	Dynamic	Static	Dynamic
RF Load		8.02	4.20		97.5	
Radiation Load			1.41		32.49	
Supports	0.60		2.40		18.0	
Input coupler	0.17	0.41	1.73	3.06	16.47	41.78
HOM coupler (cables)	0.01	0.12	0.29	1.17	1.84	5.8
HOM absorber	0.14	0.01	3.13	0.36	-3.27	7.09
Beam tube bellows		0.39				
Current leads	0.28	0.28	0.47	0.47	4.13	4.13
HOM to structure		0.56				
Coax cable (4)	0.05					
Instrumentation taps	0.07					
Diagnostic cable			1.39		5.38	
Sum	1.32	9.79	10.82	5.05	75.04	58.80
Total	11.11		15.87		133.84	

Most losses occur at frequencies where the resistance of the superconducting surfaces is several orders lower than that of normal conducting walls. Frequencies above the 1.3 GHz operating frequency and below the beam pipe cutoff are extracted by input- and HOM-couplers, but higher frequency fields will propagate along the structure and be reflected at normal and superconducting surfaces. In order to reduce the losses at normal conducting surfaces at 2 K and 4 K, the cryomodule includes a special HOM absorber that operates at 70 K, where the cooling efficiency is much higher. The absorber basically consists of a pipe of absorbing material mounted in a cavity-like shielding, and integrated into the connection between two modules. As the inner surface area of this absorber (about 280 cm^2) is small compared to that of all the normal conductors in one cryomodule, the absorber has to absorb a significant part of all the RF power incident upon it. In field propagation studies, which assume a gas-like behaviour for photons, it has been shown that an absorber with a reflectivity below 50 % is sufficient [**?**]. Theoretical and experimental studies have suggested that the required absorption may be obtained with ceramics like MACOR or with artificial dielectrics. (**Author:** *Check with current XFEL design*

for HOM absorber) (**Ed:** *This HOM absorber business was never really specifically discussed in RDR nor in this TDR elsewhere yet, either. Should describe how much extracted power we expect there and should explain the hardware and how it works by using an illustration here or in an upstream section.])* (**Author:** *Heat loads are reported in the table before. I have no access to good illustrations. If we need a specific section on HOM absorber we need a contributor for description and figures)*

It is worth noting here that a substantial effort has been performed during the Technical Design Phase for the S1-Global module and for the European XFEL Project in the consolidation and benchmarking of the static heat load assessments, as reported in Part I Section **??**. (**Ed:** *ref to Part I, scrf:cryomod)* . The S1-Global measurements show a very good consistency with heat load estimations when all conduction paths and heat transfer mechanisms are taken properly into account in the budget, indicating that the module design is well understood and proven [25]. Values for the static loads in Table 3.9 are consistent with the experience gained during the Technical Design phase; the low estimates for static losses reflect the assumption of the reduced diagnostic instrumentation foreseen for the ILC modules with respect to R&D activities as the S1-Global module tests.

The experience reported with the European XFEL prototypes has highlighted the importance of the assembly procedures in achieving nominal loads, and "training" effects for the most sensitive 2 K environment [26] (Part I Fig. **??**).

As a final remark on thermal loads, it must be noted from Table 3.9 that dynamic loads induced by RF are dominant in the 2 K region, and are intrinsically influenced by the spread of cavity performances (Q_0 values) and operating point (gradient setting). Much less experience and data is available on dynamic loads, and uncertainty factors need to be taken into account from the values reported here for their propagation into the cryosystem heat load assessments (see Section 3.5).

3.4.2.7 Shielding from magnetic field

The ambient magnetic field in the cavity region must not exceed 0.5 µT to preserve the low surface resistance. In addition to the Cryoperm magnetic shield integrated inside the helium tank of the cavity package (Section 3.3.4), the vacuum vessel is demagnetised before assembly of the cryomodule.

3.4.2.8 Quadrupole/Corrector/BPM Package

The baseline design for the ILC quadrupole/corrector/BPM package makes use of the conduction-cooled splittable quadrupole [27] developed by FNAL and KEK (Part 1 Section **??**). Fig. 3.17 shows the the magnet assembly, and the specifications are given in Table 3.10.

A key specification is the magnetic centre stability of < 5 µm for a 20% change in field strength, which is driven by beam dynamics requirements (beam based alignment).

The split-quadrupole is installed outside of the clean room around a beam pipe, thus decreasing possible contamination of the cavity RF surfaces, and greatly simplifing the string assembly operation in the clean room.

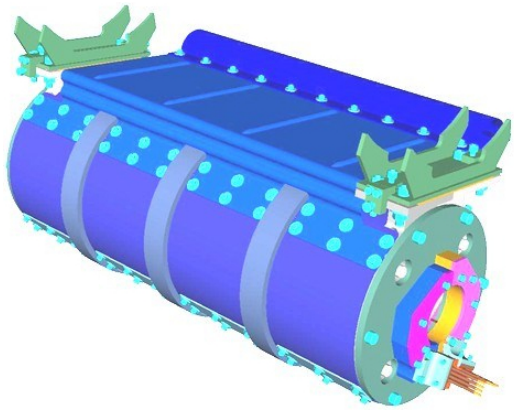

Figure 3.17. The split superconducting quadrupole final assembly.

Table 3.10. Splittable quadrupole magnet specifications and parameters.

Parameter	Value	Unit
Peak gradient	54	T/m
Integrated gradient	36	T
Magnetic stability (20% field change)	<5	µm
Peak operating quadrupole current	100	A
Magnet total length	680	mm
SC wire diameter	0.5	mm
NbTi filament size (vendor value)	3.7	µm
Cu:SC volume ratio	1.5	
Superconductor Critical current (5 T and 4.2 K)	200	A
Coil maximum field at 100 A current	3.3	T
Magnetic field stored energy	40	kJ
Quadrupole inductance	3.9	H
Quadrupole coil number of turns/pole	900	
Yoke outer diameter	280	mm

An important feature that must be addressed with the final technical design is the package fiducialization and subsequent transfer of these features to reproducible, external cryomodule fiducials to assure the correct alignment of the package with respect to the cryomodule string.

(**Ed:** *NJW: There sill needs to be something here for the 1.3 GHz cavity BPM and the corrector coils; who can provide this? Also, I note that the BPM can no longer be fiducialised together with the quadrupole in a common test stand (to estimate BPM to quad centre), since the BPM is still installed during string assembly. I'm not sure how important this is.)*

3.4.3 Cryomodule testing during mass production

For mass production, cryomodule test facilities will require large cryogenic and high-power RF infrastructure. It is expected that these facilities will be hosted and run by collaborating institutes in all three regions, possibly together with a cryomodule assembly site. While it is desirable to co-locate the assembly and test facilities, this

may prove intractable, and so it is necessary to consider the need to transport the modules (See Section 3.4.4). This is the case for the European XFEL, where the cryomodule assembly is hosted at CEA Saclay, Paris, France, while the cavity and cryomodule test facility is located at DESY, Hamburg in Germany.

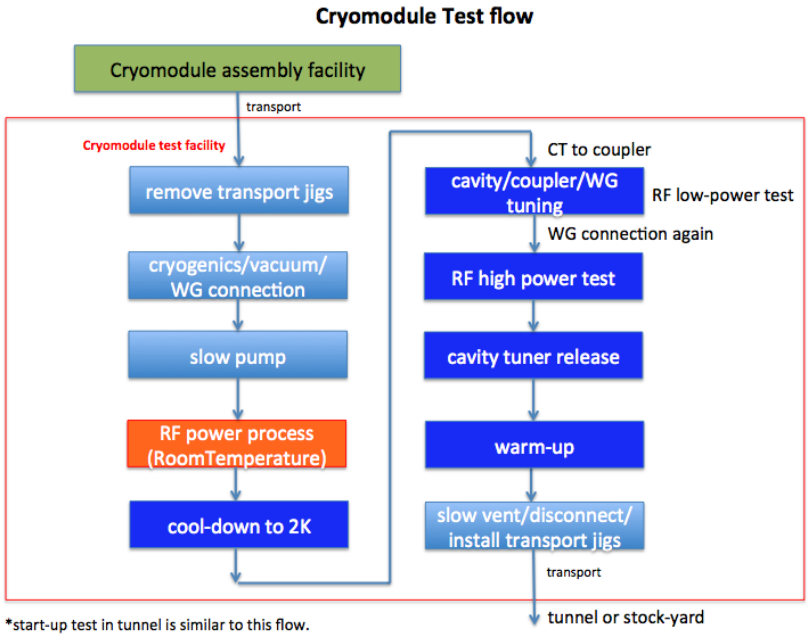

Figure 3.18. Flow chart of the cryomodule test.

Figure 3.18 illustrates the test steps for cryomodules, starting with removal of transport frames (if necessary). The cryomodule is then placed inside a concrete shielded test bay and connected to the various vacuum systems (cavity, coupler and insulation vacuum), cryogenic lines and wave-guide system. After pumping down the vacuum and performing necessary leak checks, warm RF processing of input couplers is done. The cryomodule is then cooled down to 2 K, and RF characteristics of each of cavity are measured by feeding low-power RF through a coax-rectangular waveguide converter. The parameters of the couplers and waveguides are optimised in this condition, before starting high-power RF processing of the couplers, followed by a suite of tests of the cavities at full gradient.

Validation of the cryomodule is done by confirming that all the cavities achieve the field gradient specifications of 31.5 MV/m ± 20 %, with acceptable dark current (field emission). After completing the tests, the cryomodule is warmed up with the tuner tension released. Finally the beam vacuum (cavities) are vented with argon gas.

(**Ed:** *NJW: This section is too weak in my opinion and needs much more detailed work. Especially when we consider the cost impact on the CM. We can certainly look to the XFEL test procedures for more details of exactly what tests are done and in what order. Also there needs to be some time-line showing how long it all takes (I think the XFEL currently takes 2 weeks total time). Also there needs to be some discussion here concerning the testing rate and the ramifications thereof. I believe*

our current approach is similar to the TESLA TDR, in that testing every module before installation in the tunnel is cost prohibitive, and therefore after some initial ramp up we drop to something like 1 in 3. This is more in keeping with the concept of 'production quality control'. The right thing to do is to keep a buffer of 3 CM's and if one fails, the other two must also be tested (before installation in the tunnel). If all three (or even 2/3) fail then there is a problem with the production line which needs to be remedied. We have not discussed this enough and need to do so.)

3.4.4 Shipping of Cryomodules between Regions

To date, there is limited experience on the shipping of completed cryomodules across the main regions of the ILC collaboration. FNAL shipped by air transport [28] the complete ACC39 module for FLASH (a special short module derived from the TTF design for the 3.9 GHz cavities), to DESY, where the module has been successfully tested up to its specification.

Figure 3.19. The ACC39 in its transport box upon arrival in DESY. (**Ed:** *NJW: will replace this with a picture of an XFEL prototype in its transport cradle, and then adjust the above)*

The European XFEL will report within 2015 the experience of road transportation of 100 complete modules from the string and module assembly facility at CEA/Saclay to the AMTF testing area at DESY, providing a useful statistical sample of data. Fig. **??** shows an XFEL prototype cryomodule in its transport frame. It is essential that a reliable method for overseas transport of complete modules be developed and incorporated into the final ILC cryomodule design, incorporating this experience.

3.5 Cryogenic cooling scheme

(**Ed:** *This seems to have dropped through the cracks and was missing from the original text. What follows is more or less a copy and paste from the RDR (edited to fit).* **This must be checked and updated***)*

Of the total of 1,853 SCRF cryomodules in the ILC, the 1,701 Main Linac SCRF cryomodules (92%) comprise the largest cryogenic cooling load and therefore dominate the design of the cryogenic systems. The 102 cryomodules (6%) in the bunch compressors (RTML see Chapter **??**) are considered extensions to the Main Linacs for the purposes of the cryogenic layout. For this reason, the cryogenic system is described in this chapter.

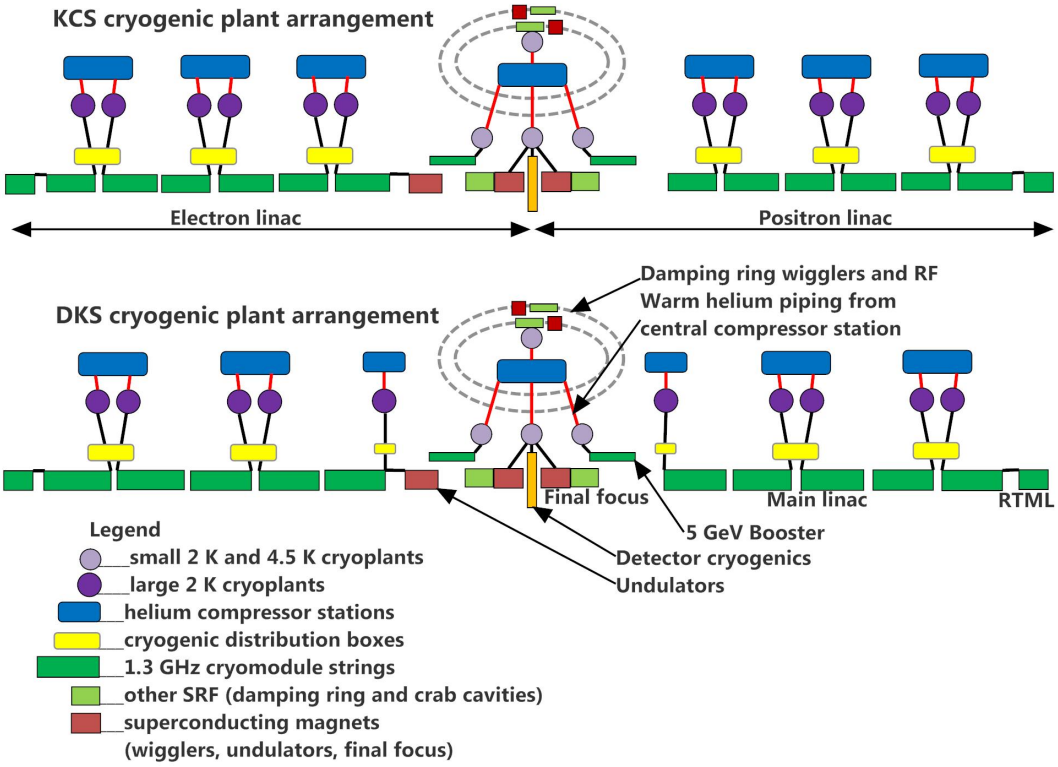

Figure 3.20. The overall layout concept for the cryogenic systems for both flat (KCS) and mountain (DKS) topography.

Figure 3.20 illustrates the the cryogenic system arrangement in ILC, which clearly shows the concept of long 2–2.5 km contiguous cryo-units, cooled by a single large 2 K cryoplant. There are detailed differences in the two site-dependent design variants under consideration, primarily driven by the choice of the RF power scheme. The most important difference is the choice of a total of 10 cryoplants for the mountain topography variant (using DKS), and 12 cryoplants for the flat topography (using KCS), as illustrated in Fig. 3.20. The total cryogenic load is however the same, but is distributed differently between the plants for the two schemes. Details of the individual segmentations for each site variant can be found inSection **??** and Section **??**.

The most upstream cryoplant in either variant also provide cooling for the 102 cryomodules in the RTML bunch compressors. The remaining loads for the the systems are cooled by separate dedicated plants in the central region as shown.

3.5.1 Cryogenic Cooling Scheme for the Main Linac

Saturated He II cools RF cavities at 2 K, and helium gas cooled shields intercept thermal radiation and thermal conduction at 5 - 8 K and at 40 - 80 K. A two-phase line (liquid helium supply and concurrent vapour return) connects to each helium vessel and connects to the major gas return header once per module. A small diameter warm-up/cool-down line connects the bottoms of the He vessels. (see Section 3.4 for more details.)

A subcooled helium supply line connects to the two-phase line via a Joule-Thomson valve once per cryo-string (9 modules or 12 modules for a short and long string respectively — see Fig. 3.2 in Section 3.1). The 5 K and 40 K heat intercepts and radiation screens are cooled in series through an entire cryogenic unit of up to 2.5 km in length. For the 2 K cooling of the RF cavities, a parallel architecture is implemented with the parallel cooling of cryo-strings resulting in operational flexibility. Consequently, each cryo-unit is subdivided into about 14 to 16 cryo-strings, each of which corresponds to either 116 m or 154 m length elementary block of the cryogenic refrigeration system, for short and long cryo-strings respectively.

Figure 3.21 shows the cooling scheme of a cryo-string, which contains 12 cryomodules (long string). The cavities are immersed in baths of saturated superfluid helium gravity filled from a 2 K two-phase header. Saturated superfluid helium is flowing all along the two-phase header for filling the cavities and phase separators located at both ends of the two-phase header. The first phase separator is used to stabilise the saturated liquid produced during the final expansion. The second phase separator in used to recover the excess of liquid, which is vaporised by a heater. At the interconnection of each cryomodule, the two-phase header is connected to the pumping return line.

The division of the Main Linac into cryogenic units is driven by various plant size limits and a practical size for the low pressure return pipe. A cryogenic plant of 25 kW equivalent 4.5 K capacity is a practical limit due to industrial production for heat exchanger sizes and over-the-road shipping size restrictions. Cryomodule piping pressure drops also start to become rather large with more than 2.5 km distances. Practical plant size and gas return header pressure drop limits are reached with 192 modules in a 16 long-string cryogenic unit, 2.47 km long.

3.5.2 Heat Loads and Cryogenic Plant Power

Table 3.11 shows the predicted heat load for a Main Linac cryo-unit comprising of 16 long-cryo-strings (a total of 192 cryomodules). Loads for other configurations can be simple scaled from these numbers.

The table lists a combined uncertainty and overcapacity factor, Fo, which is a multiplier of the estimated heat loads. The factor Fo is used to estimate a total required cryogenic plant capacity as follows. Installed cryogenic capacity

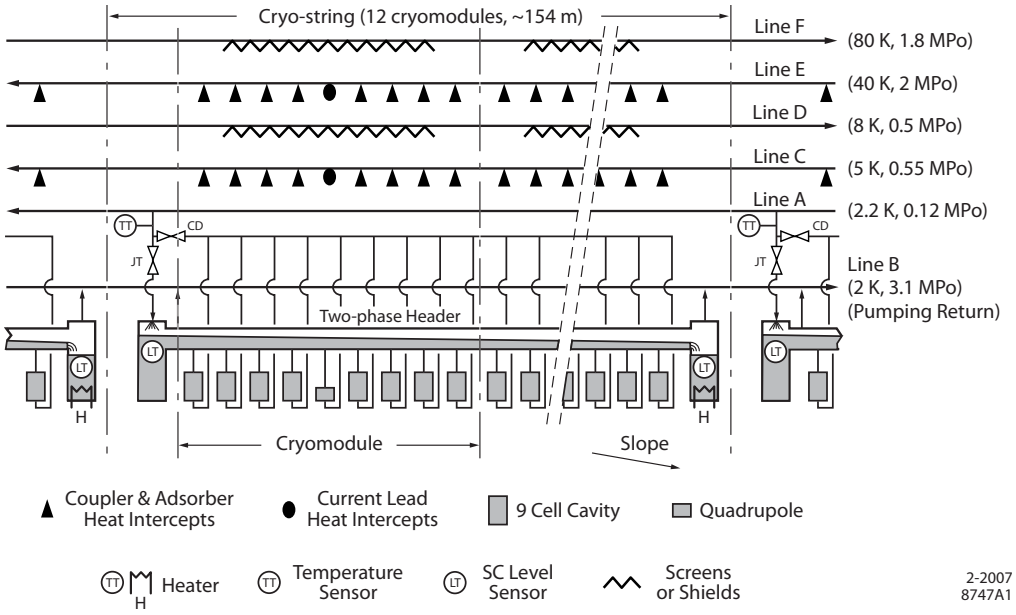

Figure 3.21. Cooling scheme of a cryo-string.

Table 3.11. Main Linac heat loads and cryogenic plant size.
(Ed: THIS TABLE TO BE UPDATED)

	40-80 K	5-8 K	2 K
Predicted module static heat load (W/mod)	59.19	10.56	1.70
Predicted module dynamic heat load (W/mod)	94.30	4.37	9.66
Modules per cryo unit	192	192	192
Non-module heat load per cryo unit (kW)	1.0	0.2	0.2
Total predicted heat per cryo unit (kW)	30.47	3.07	2.38
Efficiency (fraction Carnot)	0.28	0.24	0.22
Efficiency (Watts/Watt)	16.45	197.94	702.98
Uncertainty & overcapacity factor (Fo)	1.54	1.54	1.54
Heat Load per Cryo Unit including Fo (kW)	46.92	4.72	3.67
Installed power (kW)	771.7	934.9	2577.6
Installed 4.5 K equivalent (kW)	3.5	4.3	11.8
Percent of total power at each level	18.0	21.8	60.2
Total operating power for one cryo unit based on predicted heat (MW)			3.34
Total installed power for one cryo unit (MW)			4.33
Total installed 4.5 K equivalent power for one cryo unit (kW)			19.57

$= \mathrm{Fo} \times (\mathrm{Qd} + \mathrm{Qs})$, where Fo is overcapacity for control, off design operation, seasonal temperature variations, and heat load uncertainty. Qd is predicted dynamic heat load, and Qs is predicted static heat load. Note also that cryogenic plant efficiency is assumed to be 28% at the 40 to 80 K level and 24% at the 5 to 8 K temperature level. The efficiency at 2 K is only 20%, however, due to the additional inefficiencies associated with producing refrigeration below 4.2 Kelvin. All of these efficiencies are in accordance with recent industrial conceptual design estimates.
(**Ed:** *NJW: The RDR also included a table for the damping rings. This is currently commented out in the tex source file. However, this information should be moved to the DR chapter, if its not there already.)*

Table 3.12 summarizes the required capacities of the cryogenic plants for the different area systems. The maximum required plant capacities (equivalent at 4.5 K) are comparable with the present state of the art cryogenic plants used in the Large Hadron Collider. Total installed power for the cryogenic system is 48 MW, with an expected typical operating power of 37 MW.

Table 3.12. ILC cryogenic plant sizes (also includes sources, damping rings and beam delivery section for completeness).
(Ed: THIS TABLE TO BE UPDATED)

Area	# of Plants	Installed Plant Size (each) (MW)	Total Installed Power (MW)	Operating Power (each) (MW)	Total Operating Power (MW)
Main Linac + RTML	10	4.35	43.52	3.39	33.91
Sources	2	0.59	1.18	0.46	0.92
Damping Rings	2	1.26	2.52	0.88	1.76
BDS	1	0.41	0.41	0.33	0.33
Total			47.63		36.92

3.5.3 Helium Inventory

As illustrated in Figure 3.22, most of the helium inventory consists of the liquid helium which bathes the RF cavities in the helium vessels. The total helium inventory in ILC will be roughly equal to that of the LHC at CERN, about 650,000 liquid liters, or about 100 metric tons.

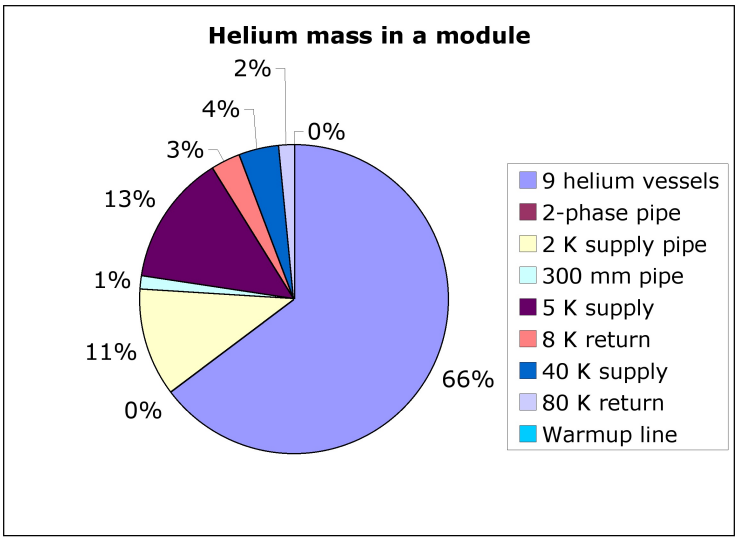

Figure 3.22. Helium mass in a module.

Table 3.13. Main Linac helium inventory.

Volumes		Helium (liquid liters equivalent)	Tevatron Equiv.	LHC Equiv.	Inventory Cost (k$)
One module		370			
String	12 modules	4,500	0.1		13.4
Cryogenic unit	14-16 strings	68,000	1.1	0.1	203.6
ILC Main Linacs	2x5 cryo units	680,000	11.3	0.9	2,037

3.6 RF power source

3.6.1 Overview

Table 3.14. Main parameters relevant to the RF power that is required for one 9-cell cavity. The RF power numbers are intended to give an indication of the power required, represent the ideal match conditions, and do not include overheads for controls, waveguide losses or the expected spread in operating gradients.

Parameter	Unit	Value for baseline
RF Frequency	Hz	1.3
Beam current in the pulse	mA	5.8
Accelerating gradient	MV/m	31.5
Cavity length	m	1.038
Q_L (matched)		5.5×10^6
RF Voltage	MV	32.7
Beam phase	deg	5
RF pulse length	ms	1.65
Beam width	ms	0.72
Filling time	ms	0.93
Repletion rate	Hz	5
RF power into cavity	kW	188
RF for 26 cavities	MW	4.9
RF for 39 cavities	MW	7.3

The centrepiece of the RF power system is the 10 MW multibeam klystron (MBK). With the power required by each cavity including a certain overhead for power loss in the waveguides and allowance for tuning, The MBK provides enough peak power in the pulse to drive up to 39 cavities under the nominal beam loading conditions (see Table 3.14).

As described briefly in Section 3.1, the two site variants (flat and mountain topography) differ significantly in how the MBK power is supplied to the cavities in the tunnel.

For the flat topography, the Klystron Cluster Scheme (KCS) is the preferred solution, where all the MBKs, modulators and associated DC power supplies, are installed in "clusters" within buildings on the surface. The RF power from each cluster of klystrons combined, which is of the order of 200∼300 MW, and transported through over-sized circular waveguides to underground linac tunnels.

For the mountain topography, such as those sites considered in Japan, a more traditional Distributed Klystron System (DKS) approach is taken where the klystrons are distributed along the main linac tunnel, with each klystron connected directly to 39 cavities (4.5 cryomodules). In this case the tunnel will have a wide flat-bottomed cross section shape referred to as "kamaboko"[2]. The tunnel is divided along its length by a thick, concrete radiation shield into two parallel corridors – one for cryomodules and the beamline, the other for klystrons, DC power supplies and control hardware.

[2] A Japanese fish cake which resembles the tunnel cross section.

This section gives focused descriptions on aspects of the component of the RF power system and Low-level RF (LLRF) control that are common to both flat and mountain sites. Details specific to the KCS and to the DCS are given in Chapter **??**(**Ed:** *mlflat)* and Chapter **??**,(**Ed:** *mlmtn)* respectively.

3.6.2 Modulator

(**Ed:** *NT 20120901 - Still need readjustment of topics to cover in TDR1 and TDR2.)*

To generate the flat, high voltage pulses required by the 10 MW klystron rf power source, a Marx modulator is adopted in the ILC design. The maximum output power requirements for the modulator are 120 kV, 140 A, 1.6 ms pulses at a 10 Hz repetition rate[3]. In Table 3.15, the modulator specifications are listed for driving a klystron producing a peak output power of 10 MW with a microperveance of 3.38 and an efficiency of 65 %.

Table 3.15. Parameter specifications for the klystron modulators of the main linacs of ILC.

Parameter	Unit	Specification
Output voltage	kV	120
Output current	A	140
Pulse width	ms	1.6
Pulse repetition frequency	Hz	5 (10)
Average power	kW	134
Output pulse flat-top	%	±0.5
Pulse-to-pulse voltage fluctuation	%	±0.5
Energy deposited into klystron during a gun spark	J	< 20

The Marx modulator uses solid-state switches to charge capacitors in parallel during the interval between output pulses. During the output pulse, the capacitors are discharged in series to generate a high voltage output with a magnitude of the charging voltage times the number of stages. With this topology, low-voltage components can be used to produce a high-voltage output without requiring an output transformer. There are several ways one may produce a flat output pulse. One method is to integrate a "buck converter" in series with each cell which uses a closed-loop correction scheme to produce a square output pulse for each cell. A diagram of a Marx modulator and the circuit of one simple Marx cell are shown in Fig. 3.23.

There are several advantageous characteristics of the Marx topology. The modular design simplifies fabrication and allows redundant hardware to be implemented. Solid-state switching is intrinsically long-life, and in conjunction with redundant hardware, a high-availability architecture is possible. Modularity reduces the spares inventory and simplifies maintenance, thereby reducing the mean time to repair. Due to the absence of a high voltage output transformer, short rise and fall times are possible, further increasing efficiency. (**Ed:** *[Burkhart 2010 IPAC reference])*

[3]For the 10-Hz mode operation for positron production.

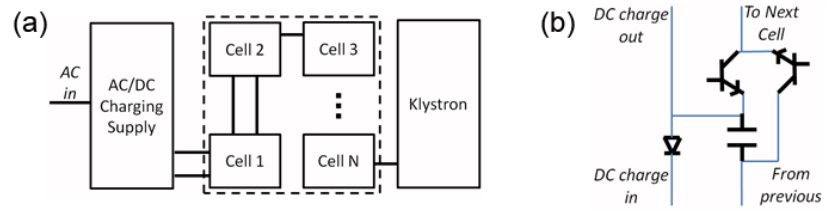

Figure 3.23. a) Simple block diagram of a Marx modulator and b) simple single cell circuit.

Multiple R&D programs have been pursued to develop and demonstrate the efficacy of a Marx-topology modulator to drive the ILC klystron. The requirements and many technical advantages are discussed in Part I, Section **??** (**Ed:** *There appears to be no specific section on the Marx R&D in the outline of Part I)* As described there, in 2007, the U.S. DOE supported four Marx modulator development plans. All four projects resulted in full-scale prototypes, some of which are pictured in Fig. 3.24, thereby demonstrating the technical feasibility of a Marx-topology modulator.

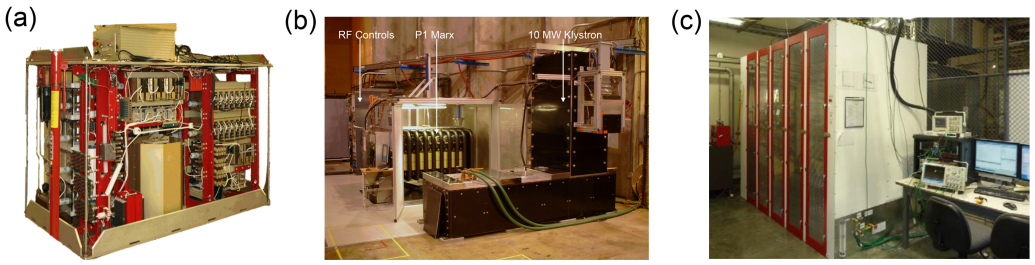

Figure 3.24. DTI Marx modulator, b) SLAC P1 Marx modulator and c) SLAC P2 Marx.(**Ed:** *todo: insert figures using subcaptionbox)*

The SLAC P2 Marx is an embodiment of the Marx topology which has many advanced features and is utilized for costing for the ILC. It contains thirty-two identical cells, with $N + 2$ redundancy. Pulse top flatness at the $\pm 0.05\%$ level has been demonstrated with operation into a water load. A full pulse waveform of this Marx and the flatness are shown in Fig. 3.25. The flat pulse is generated using a closed-loop regulation scheme which feeds forward on both the voltages of the individual cells as well as the overall output voltage. In addition, the cells are phase shifted to stagger the ripple of each individual cell with respect to each other. In doing so, they substantially cancel to produce an overall low modulator ripple.

Very fast rise and fall times of less than 15 µs were obtained with the water load, corresponding to 0.5 % of the total energy output from the Marx, which is dissipated in the klystron collector, which leads to a high efficiency.

The AC/DC charger technology has a low technical risk but its performance is important in achieving a cost-effective and efficient RF system. A survey of available technologies indicates that a conversion efficiency of 95 % is realisable, and this is assumed in the heat loading values presented in Table 3.16.

Additional characteristics of the SLAC P2 Marx include the use of air insulation

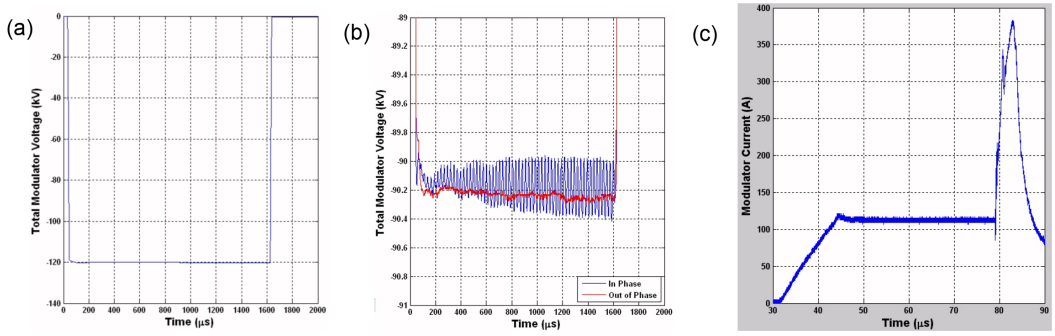

Figure 3.25. a) Output pulse waveform from Marx, b) flatness of the flat-top and c) measured modulator current pulse before and after an arc. (**Ed:** *NT - axis labels are too small!)*

Table 3.16. Power efficiencies and heat load of Marx modulators.

Parameter	Unit	Specification
SLAC P2 Marx DC to pulse flattop efficiency	%	95 ± 1
Assumed charging supply AC to DC efficiency	%	95
Usable power delivered to klystron	kW	134.4
Power delivered to collector during pulse rise and fall (assuming 10 μs rise and fall)	kW	0.5
Power delivered to collector during pulse rise and fall (assuming 200 μs rise and fall)	kW	9.6
Power dissipated to air inside of modulator enclosure	kW	7.1
Power dissipated in the DC chargers	kW	7.4

and cooling rather than oil. At the marginal expense of compactness, air insulation simplifies maintenance, reduces hazardous waste containment issues, and simplifies component compatibility. Waste heat is transferred the modulator via an air to water heat exchanger.

The SLAC P2 Marx also utilizes an intelligent control system with embedded diagnostic and prognostic systems. These can be used to monitor cell activity in real time and to anticipate the onset of components' end-of-life phase. Twelve, 12-bit, 1 MS/s ADC are used within each cell to monitor voltage, current, and temperature values of interest. These are used in the closed loop regulation scheme and also can be used to troubleshoot the cells in-situ.

Fault susceptibility is another important characteristic. It is necessary not only to prevent damage to the modulator, but also to protect the klystron in the event of a gun arc. The Marx satisfies these requirements. Figure 3.25 c) shows the current waveform from a simulated klystron arc event performed using a self-break spark gap. It shows that the IGBT opened with a 0.5 µs delay after sensing the arc, suppressing the energy deposited to less than 10 J, satisfying the requirement for klystron protection. In addition, if a main IGBT fails in the Marx during a gun spark event, the charge IGBT in the cell closes. In this way, the energy within the cell is contained in the cell and is not transferred to the klystron.

The majority of the capabilities of the P2 Marx have been demonstrated. However, to adequately characterize the mean time before failure and the mean time to repair, an extended testing and qualification period is necessary.

3.6.3 10 MW Multi-Beam Klystron (MBK)

(**Ed:** *NT: I have freely touched this section up. I tried not to introduce errors, but I may have. Please, check.)*

The RF power to drive the accelerating cavities at the ILC is provided by 10 MW L-band klystrons, whose baseline design is based on a multi-beam scheme. In case of the multi-beam klystron (MBK) for the ILC, the electron current is split into six beams of low perveance. This arrangement allows a reduction in the beam voltage and to weaken the space-charge effect at the same time, the net result of which is to achieve an improved power efficiency with a lower-voltage modulators, all of which fit within a smaller installation footprint. Table 3.17 gives the main parameters for the MBK.

Table 3.17. 10 MW MBK Parameters.

Parameter	Specification
Frequency	1.3 GHz
Peak power output	10 MW
RF pulse width	1.616 ms
Repetition rate	5.0 (10) Hz
Average power output	78 kW
Efficiency	65 %
Saturated gain	$>$ 47 dB
Instantaneous 1 dB BW	$>$ 3 MHz
Cathode voltage	$>$ 120 kV
Cathode current	$<$ 140 A
Filament voltage	9 V
Filament current	50 A
Power asymmetry	$<$ 1 %
Lifetime	$>$ 40,000 hours

The design effort for the 10 MW-class MBKs began around the time of TESLA conceptual design and has evolved through the European XFEL project. Vertically mounted prototypes were initially developed by a few electron tube manufacturers and successfully achieved the 10 MW goal. They were followed by horizontally mounted MBKs, whose builds are compatible with implementation at the European XFEL and ILC. They have successfully demonstrated the same RF power performance as the vertical models. DESY, KEK and SLAC have all procured and operated these MBK's, evaluated their performance and obtained satisfactory results.

The current MBK designs are now relatively mature. All vendors have provided suitable solutions for the resonant cavities within the klystron body and beam focusing. Figure 3.26 shows photographs of two L-band MBK's from two different vendors (Thales and Toshiba). Typical performance data is shown in Fig. 3.27.

A crucial aspect for operations of the ILC linacs is the lifetime of the klystrons. The MTBF for the ILC klystrons is specified at $\geq$40,000 hours. The lifetime for linear

Figure 3.26. Thales TH1801 and b) the horizontally mounted Toshiba E3736.

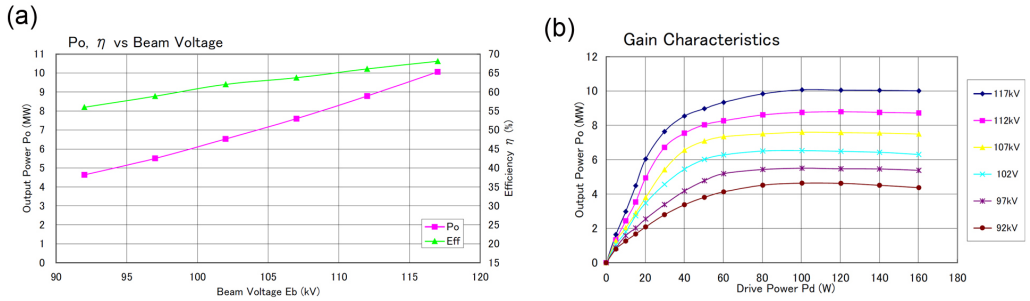

Figure 3.27. Measured performance data of (**Ed:** *which klystron?)* , showing (a) output power and efficiency as functions of beam voltage and (b) gain characteristics.

beam tubes is dominated by the durability of the cathode. With cathode loading as low as 2 A/cm^2 achieve by some vendors, the expected (theoretical) lifetime is in excess of 50,000 hours. However, operational experience is required in order to estimate the true lifetime. Lifetime tests are planned, and the ∼30 MBKs required for the European XFEL will also provide significant input.

The manufacturability of MBKs is an important issue, since the ILC requires nearly 500 tubes to be prepared within a period of 5 to 7 years. The investment in RF test and processing infrastructure by industry is likely to be cost prohibitive for production at this scale. A more cost-effective model would be for collaborating instates ("hub laboratories") to host such facilities and provide the manpower.

3.6.4 Local power distribution system

The arrangement and installation of waveguides near the cryomodules is the same in both cases for the KCS and DKS, and is commonly referred to as the Local Power Distribution System (LPDS). The design of the LPDS needs to satisfy two important design criteria:

- It must provide a cost-effective solution to distributing the RF power to the cavities with minimum RF loss;

- It must provide flexibility to remotely and independently adjust the power delivered to each individual cavity to allow for the expected ±20% spread in gradient performance.

Furthermore it was desirable to keep as far as possible a common design between DKS and KCS, and — in the case of DKS — provide a relatively straightforward reconfiguration to 26 cavities per klystron required for the luminosity upgrade (Section **??**).

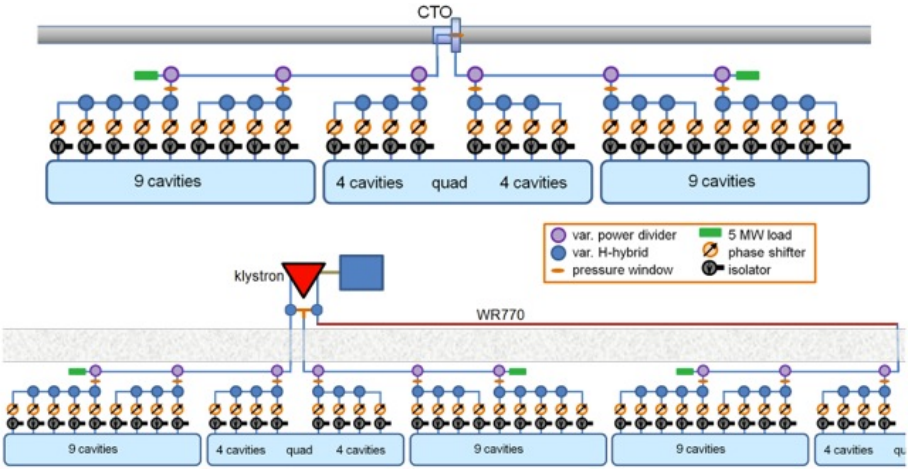

Figure 3.28. Schematic of the Local Power Distribution System (LPDS) which delivers RF power to accelerating cavities in the main linacs. (a) shows the case of the KCS option, and (b) shows the case of the DKS option. In both cases each LPDS input feed drives 13 cavities. (Reproduced from Fig. 3.1 in Section 3.1.) (**Ed:** *NT: Please touch up the figure and add labels (a) and (b).*
NJW: this figure now appears twice, but I have also referenced in back. May find different.)

Figure 3.28 shows schematics of distribution of RF power onto cavities in the cryomodules. Each LPDS drives 13 cavities, and is capable of handling and distributing up to 5 MW of input power. For the KCS (Fig. 3.28(a)), two such LPDS distribute the RF power from one CoaxialTap-Off (CTO) connected to the high-power overmoded waveguide to 26 cavities (one ML unit). For DKS, three LPDS feeds are used to drive a total of 39 cavities from one single 10 MW klystron (Fig. 3.28(b)).

The LPDS divides its input power to 13 cavities as shown in Fig. 3.28. This is accomplished by first using two power dividers in series, to effectively divide the power in the ratio of 4:4:5 (assuming equal power to all cavities). Ideally the first divides the input power by 4:9, while the second divides the remaining power by 1:1. At the next level of the distribution, the power is further divided up in a similar cascaded fashion using H-hybrids, to each of the four (five) cavities (e.g., in the ideal ratios of 1:4, 1:3 and 1:2 for each H-hybrid in a four-cavity branch).

Figure 3.29 shows a CAD model of a 13-cavity unit of the LPDS. To accommodate the expected ±20% random cavity gradient performance, the LPDS has to allow for unequal feeding of RF power into individual cavities. The solution adopted by the LPDS is to use variable power dividers (VPD) and variable hybrids, which allow the remote adjustment of the cavity power as required.

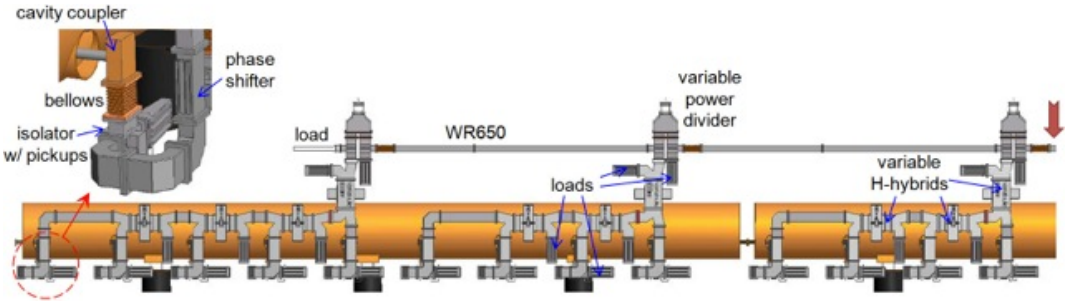

Figure 3.29. CAD model of a 13-cavity unit of the Local Power Distribution System (LPDS)

Figure 3.30 shows a schematic illustration for an entire VPD and a picture of its U-bend phase shifter prototype. The design of the U-bend shifter features an inner waveguide which can be moved like a trombone by an external motor [8]. The VPD forms a 4-port device which, with a load on one port, allows full range adjustment of power division between the forward waveguide and the downward extraction waveguide. By moving the phase shifters in opposite directions, the phases of the outputs can be held fixed, allowing a pure amplitude control. With each VPD extracting the prescribed amount of power required for the cavities assigned to it, excess power is directed into a 5 MW load at the end of the upper waveguide. On each extraction port, a thick ceramic block window separates the higher power system above, pressurised with two atmospheres of dry air or nitrogen, from the unpressurised, lower power region below.

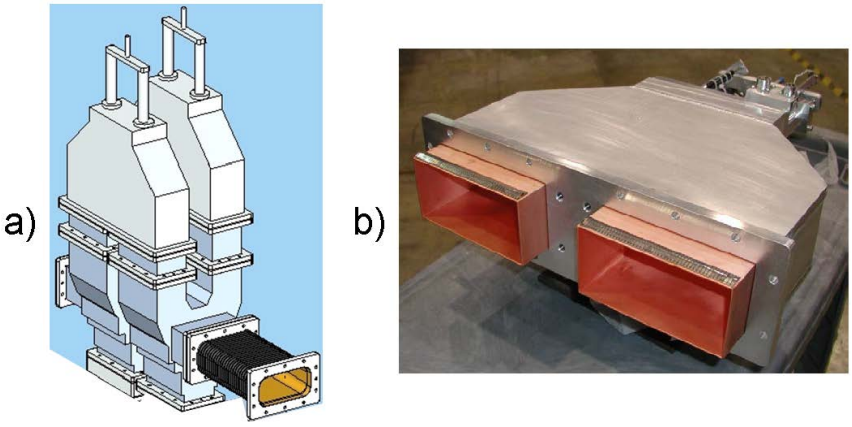

Figure 3.30. Illustration of the variable power divider composed of two folded magic-T's and two U-bend phase-shifters. b) Photograph of a mitered H-plane U-bend phase shifter with fingerstock to contact the mating waveguide.

Figure 3.31 shows the geometry of a variable H-hybrid [9, 10], its field pattern and in-line port design modification . The interior of this 4-port hybrid accommodates two modes, and their relative phase lengths (and thus the power split) can be changed by shifting the locations of "pontoon"-like objects by means of a pair of motorised supports.

(**Ed:** *NT: Neither papers by Fukuda and Nantista really explains this variable 4-port in too much details.)* (**Ed:** *JC,CN,CA,MR: refer to the S1-Global report)*

In case of an in-line version, the "H" port configuration is modified to fit the layout, as shown by the right-most illustration in Fig. 3.31. The first in each set is oriented vertically to avoid mechanical interference. Again, the fourth port of each divider is load-terminated. While not intended for a full range, this arrangement achieves splitting ratios which considerably deviate from the nominal (1/5,) 1/4, 1/3, and 1/2 divisions.

Adjustment of the power splitting with this variable hybrid affects both the phase and the amplitude. Therefore, a WR650 motorised phase shifter (adjusted via either a movable wall or "pontoon") is included in the waveguide feed leading to each cavity.

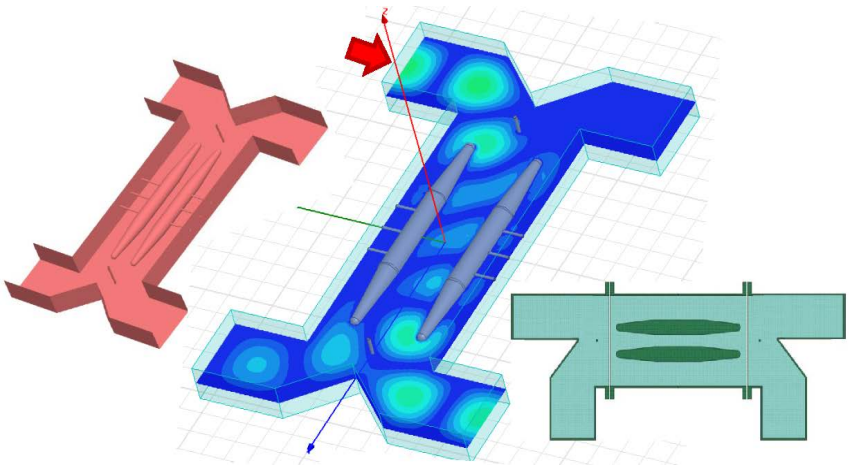

Figure 3.31. Variable H-hybrid geometry, sample field pattern and in-line port design modification. Moving the two suspended conductors in and out perturbs the relative phase between the two modes supported in the interior section, resulting in a varying power split at the output ports.

Incorporated in each cavity feed is a ferrite-based isolator, or circulator with load. This is required to prevent the power that is reflected or discharged due to the pulsed standing-wave cavities from re-entering the waveguides. Pickups at the input and load ports of the isolators provide the low-level RF control system with information on the forward and reflected cavity voltages.

(**Ed:** *NT: Note: "cavity signals" or "rf power" ?)* Finally, a flexible bellows connects to the input box ("door knob" box) at the warm end transition of the input coupler of the cavitySection 3.3.1. The LPDS additionally includes a number of bends, waveguides and spacers, as well as a few semi-flexible sections in the upper region to facilitate installation and relieve stress.

3.6.5 RF Power Requirements

In order to estimate the total (minimum) number of klystrons required, it is necessary to take into account all the expected RF losses along the entire RF power waveguide delivery system to the cavity. A further 'inefficiency' can be attributed to the random

spread in cavity gradient performance, since in general it is not possible to perfectly match all the cavities connected to the same power source, since the RF pulse and hence the fill time must be the same for all cavities [**?**]. This results in reflected power from (most) of the cavities. Finally, some small fraction of klystron power is required for LLRF control.

While estimation of the distribution system losses and control overhead is relatively straightforward, estimation of the impact of the cavity gradient spread can only be described in a statistical sense, since it is currently assumed that there is no possibility to sort the cavities during manufacture and installation into the cryomodules, resulting in an effectively random cavity distribution in the linac. The approach adopted here is to use monte carlo techniques by running many random seeds, and taking the 95% percentile limit of the power required. Details of the calculation can be found in [].

Table 3.18 traces the RF power budget from the cavities back to the klystrons for both DKS and KCS. The effect of the random cavity gradients are responsible for the first increase in the table. Some post-installation adjustment of the high-level power division (fine-tuning or changing CTO's and hybrids) is assumed in order to limit this to a few percent (the lower-level PDS is more generally tailorable). The first number (extra beam power) reflects the statistical fluctuation of the total voltage of the cavities driven by the single source (the source must be able to accommodate the highest voltage, at least at the 2σ level). The next effect (reflection) is due to the mismatch of the individual cavities arising from the constant fill time as mentioned above. This represents a real operational power that is dumped in the loads. Folded into this number is about 0.8 % to support a 5° RF-to-beam phase. 7 % overhead (5 % usable) is allotted for LLRF manipulation, and 8 % for average losses in the components of the waveguide circuit that provides local distribution of the power along the cryomodules.

Beyond the local PDS, the accounting diverges for the two options. DKS has additional losses in the WR650 shielding penetrations and dividing/combining components, as well as in the WR770 waveguide run supplying power for half a ML Unit to the vacant klystron position. KCS, of which there are two system types of slightly differing size, naturally has more losses, since power is brought from above ground. The estimate includes the average loss along the main circular tunnel waveguide (assumed to be copper plated) to each tunnel CTO, the loss in the bends and shaft waveguide, and the loss along the surface main waveguide and combining CTO string. The latter includes a circular WC1375 waveguide run past an area where additional klystrons can be installed for a beam power upgrade. Finally, there is loss budgeted for the waveguide connections from the klystron output ports in through the outer region of the CTO. A major contributor here is the 5 MW isolators required to protect the klystron from the reverse power it could see from the combining circuit, e.g., 10 MW if it fails. Although this economical designs leaves little room to spare, the calculations suggest they are consistent, in each case, with the 10 MW specification on the klystron. The numbers represent peak power availability required at maximum beam energy, based on estimated system losses and the expected spread in cavity performance.

Table 3.18. RF power budgets for KCS and DKS local power distribution systems

		KCS		**DKS**
Cavity and Local Power Distribution		(kW)		(kW)
Mean beam power per cavity		*189.18*		*189.18*
Extra beam power for ±20% gradient spread	2.90%	194.67	5.30%	199.21
s.s. reflection for ±20% gradient spread	6.00%	206.35	6.00%	211.16
Required LLRF overhead	7.00%	220.8	7.00%	225.95
Local PDS average losses	8.00%	240	8.00%	245.59
Multiply by number of cavities fed as a unit	26	6239.9	39	9578.1
Required local PDS RF input power		*6239.9*		*9578.1*
Power Combining & Transport (DKS)				(MW)
RF power to local PDS				*9.578*
Combining/splitting and shielding penetrations			1.10%	9.6847
WR770 run loss/3			1.40%	9.8222
Required power from klystron (DKS)				*9.822*
Power Combining & Transport (KCS)		(MW)		
RF power to ML Unit		*6.2399*		
Multiply by number of ML Units per KCS	26 (25)	162.24 (156)		
KCS main waveguide loss	5.0% (4.7)	170.78 (163.69)		
Shaft and bends loss	1.80%	173.91 (166.69)		
CTO string and upgrade WC1375 run loss	1.50%	176.55 (169.23)		
Klystron waveguide into CTO	5.60%	187.03 (186.74)		
Divide by number of klystrons	19 (18)	9.8436 (9.9594)		
Required power from each klystron (KCS)		*9.844 (9.959)*		

3.7 Low-level RF (LLRF) control concept

3.7.1 Introduction and overview

(**Ed:** *NT: Somewhere at the very beginning we should explain why we have to do this sophisticated LLRF control this way. The points to articulate may include:*

1. ~~*The cavities have performance variations and they need to be operated at different field gradients in the presence of beam loading so their operation have to be balanced to give flat energy gains across each bunch train*~~ *(**Ed:** JC,CN,CA,MR: made note in LLRF section to reference cavities section where it describes the cavity production gradient distribution)*

2. ~~*Requirement specifications on the flatness of the energy gain across the bunch train is dictated by beam dynamics consideration, i.e. emittance control*~~ *(**Ed:** JC: it's now referenced from this section. There's a note in 3.1 to include some text about this)*

3. ~~*This LLRF business has to be done under the constraints of limitation of individual cavity gradient performance and the total power available from the RF power sources.*~~*(**Ed:** JC: This is already noted in the description of requirements. An RF power budget table from Chris N has been added. Chris is is writing an explanation of the table for inclusion)*

4. ~~*The signals to feed back on have to come from reflected and transmitted power on individual cavities, not from the beam energy or orbit, since adequate control must be applied on the basis of individual RF units*~~ *(**Ed:** JC: yes, we need fwd and reflected power, but the regulation of gradient is done on the field probe signals. I added a note about acquiring the fwd and reflected power signals. There is already a note about not using beam-based feedbacks)*

This particular section may not have to give a thorough discussion on all of them here, but the TDR as a whole has to. And this section has to give appropriate pointers to them)

The primary function of the main linac and RTML LLRF systems is to control the phase and amplitude of the klystron forward power so that the required cavity fields are reached at the end of the fill time and thereafter remain stable for the duration of the beam pulse. Since many cavities are fed from each individual klystron (or cluster in the case of KCS), the LLRF system regulates the vector sum of all the cavity fields controlled by that klystron (or cluster). Table 3.19 shows the allocated phase and amplitude tolerances on the cavity field vector sums. These are derived on the basis of a maximum allowable 2 % loss in luminosity or 0.1 % change in energy at the exit of the linac resulting from cavity field errors. Since the tolerances take into account the ensemble of cavities in each linac, they are more stringent for common-mode errors than for errors that are uncorrelated between cavities. Beside stabilising the cavity field vector sums, the LLRF systems must also achieve flat fields in each individual cavity. The 1 % rms tolerance on cavity gradient flatness is driven by two separate criteria: 1) the requirement to operate cavities within a few percent

of their gradient limits; and 2) beam dynamics criteria for minimising single bunch emittance growth (see Part I Section **??** (**Ed:** *Table* **??***)*).

Table 3.19. Tolerances for cavity field vector sum phase and amplitude.

	Phase (degree)		Amplitude (%)	
Error type	Lum. (%)	delta-E(%)	Lum. (%)	delta-E (%)
Bunch-compressor (correlated)	0.24	0.35	0.5	1.8
Bunch-compressor (uncorrelated)	0.48	0.59	1.6	2.8
Linac (correlated)	large	0.36	large	0.07
Linac (uncorrelated)	large	5.6	large	1.05

(**Author:** *See Kubo's section in TDR1/AS for specs)* (**Author:** *The specs come from Kubo's section in TDR1/AS table tab:mlrfjitter Dynamic Errors ML RF)*

The LLRF system must accommodate several critical constraints coming from the design of the main linac, specifically:

- all cavities must run reliably at up to 95 % of their gradient limits in order to reach the linac design energy of 250 GeV;
- the ±20 % spread in the above limits;
- klystrons will run at up to 95 % of their rated forward power if the linacs are operating at the maximum design energy and beam current.

3.7.2 Vector-sum control of cavity fields

The LLRF system design is based on the digital controller implemented at FLASH and that will be used on the European XFEL [](**Ed:** *add ref)* . Similar systems have also been implemented at STF at KEK [](**Ed:** *add ref)* and NML at Fermilab [](**Ed:** *add ref)* . The main functional elements are illustrated in Fig. 3.32 [34].

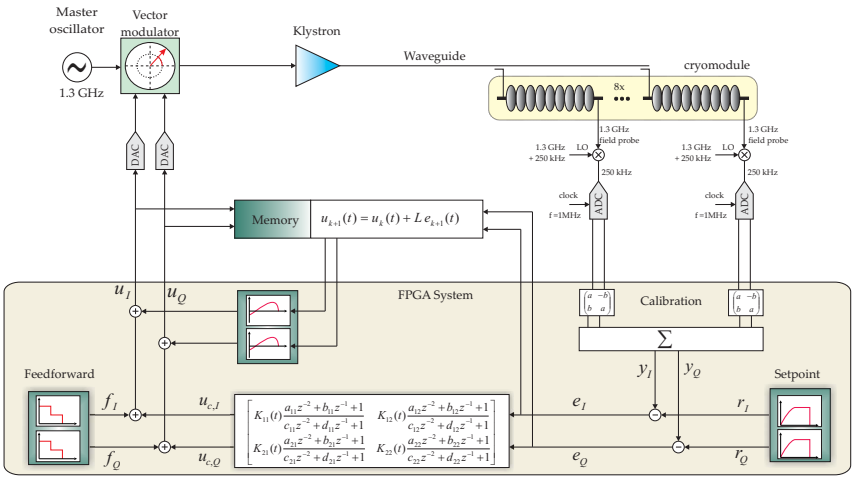

Figure 3.32. Block diagram of the digital LLRF control system at FLASH (for clarity, only one cryomodule is shown)

Cavity field probe signals are down-converted to an intermediate frequency (IF) and directly acquired by ADCs in the LLRF controller. The data-stream from the ADCs is separated into in-phase and quadrature terms and a complex cavity field vector-sum is computed for comparison with the required vector sum in order to produce an error term for the regulator. The controller output is converted to analog signals (DAC) connected to a vector modulator that varies the amplitude and phase of the 1.3 GHz master oscillator RF reference signal to the klystron. The controller output to the klystron comprises two components: a feed-forward term that is determined a-priori using knowledge of the required cavity field profile and the expected beam current profile; and a correction term is generated dynamically by a feedback regulator.

In addition to acquiring the cavity field probes for vector-sum control, cavity forward and reflected power signals are also acquired for use by high level control applications.

3.7.2.1 Feed-forward controller

Due to the very low-bandwidth of the super conducting cavities and delays in the closed loop system, dynamical feedback alone is not sufficient to completely suppress high-frequency distortions or to achieve zero steady-state errors. However, effects that are directly correlated with the 5 Hz pulse structure and that are repeatable from pulse to pulse can be pre-emptively compensated using feed-forward, leaving smaller residual and non repetitive disturbances to be compensated using the closed- loop feedback regulator. A learning feed-forward system is used to iteratively adjust the shape of the feed-forward waveform in order to compensate for repetitive pulse-to-pulse errors, leaving the intra-pulse feedback system to attenuate pulse-to-pulse jitter and intra-pulse fluctuations.With knowledge about field imperfections in previous pulses, the residual control errors can be minimised. Optimisation of the learning feed-forward system is performed by a model-based learning feed-forward algorithm

3.7.2.2 Feedback regulator

There are many potential sources of jitter that must be compensated by the feedback regulator, but the primary sources of jitter are expected to be:

Microphonics: external mechanical vibrations can be transferred to the cavities via the supporting system within the cryostat. Modulation of the resonant frequency due to microphonics is estimated to be ∼10 Hz rms(**Ed:** *check value)* . (**Ed:** *JC: In cavity integration table specs of the tuners, the number is 50Hz)* The dominant sources of vibration that cause microphonics include flow of cryogenic fluids through the cryomodule, vibration from mechanical pumps and water systems, and ground motion.

AC power-line disturbances: such as fast voltage spikes, voltage dips or surges, voltage harmonic distortion, changes in fundamental frequency, or jitter in the phase of the fundamental frequency.

Thermal drift: small changes in cable lengths, technical equipment working points, etc. can result from changes in the ambient temperature or in tech- nical

equipment thermal loads during machine ramp-up or ramp-down. While these effects can be reduced by careful system design, they cannot be eliminated and must therefore be compensated using feedback.

The feedback regulator uses a multi-variable, second-order controller whose coefficients are automatically tuned by model based controller methods. It's primary function is to attenuate random pulse-to-pulse and intra-pulse jitter. A more detailed description of the FLASH LLRF system algorithms can be found in [34]. It is worth noting that the FLASH LLRF system makes extensive use of intra-pulse beam-based feedback for additional regulation, specifically bunch arrival time, compression, charge, and energy. Such extensive use of beam-based feedback is not possible in the ILC Main Linac due to the limited availability of intermediate diagnostics. There is however, a priori knowledge of the bunch by bunch charge since it is measured in the Damping Ring prior to extraction.

As noted in Section 3.6.5, when the linac is operating at the maximum nominal energy and beam current, the klystrons will operate close to the limits of their rated output. In this operating region, the klystron characteristics are highly non-linear, a lineariser function must be applied to the klystron control signals before they are converted to the analog domain.

3.7.3 Individual cavity control

While the vector-sum controller regulates the net sum (or equivalently the average) of the cavity fields, the fields in individual cavities are not constrained. Indeed, regulating the vector sum causes any anomalous effects on individual cavities to appear out of phase on every other cavity. To optimise the setup of individual cavities, high level functions in the LLRF system adjusts coupler positions, RF power dividers, and fast and slow tuners, giving control of the resonant frequency, forward power ratio (P_k), and Q_{ext} respectively for each cavity.

The most important control functions at the individual cavity level are compensating Lorentz-force detuning and establishing flat cavity gradients in the presence of beam loading.

3.7.3.1 Lorentz-force detuning compensation

When there is rf field in the cavity, the cavity walls experience electrostatic and magnetic forces that act to distort the cavity shape and shift the resonant frequency of the cavity. The magnitude of the detuning (Δf) due to these Lorentz forces is proportional to the square of the field in the cavity (E_{acc}). Since the cavity and its support structure form a mechanical system with mass, the detuning effect of the Lorentz forces does not occur instantaneously, but instead increases over the duration of the pulse. Fig. 3.33 shows detuning over the duration of the rf pulse for different cavity fields [37].

This Lorenz-force detuning must be compensated in order to maximise the RF power efficiency and to reduce the electric fields at the cavity input coupler, as well as maintaining constant voltage on individual cavities during the beam pulse. This is accomplished using the fast piezo actuators that are integral to the cavity

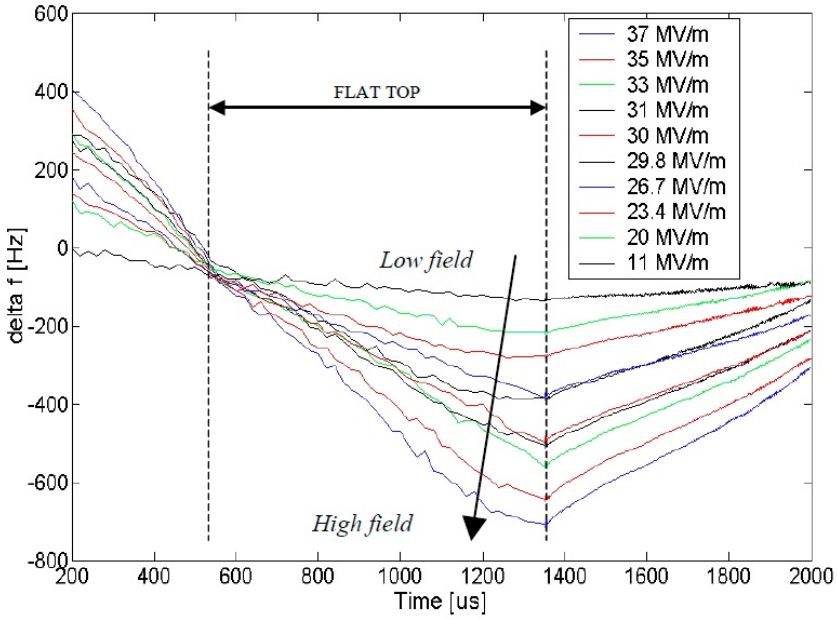

Figure 3.33. Cavity detuning during RF pulse as a function of gradient

tuning mechanism (Section 3.3.2). Two different approaches have been successfully demonstrated to determine an appropriate drive signal for the piezo tuners [36, 35]. Both methods use the piezo tuners to preemptively put the cavity structure into motion before the RF pulse in such a way to cancel the effect of the Lorentz forces. The methods rely on indirect observations of the cavity detuning inferred from the measured forward and reflected power waveforms.

3.7.3.2 Control of cavity gradient flatness

(**Ed:** *NJW: punted on trying to explain PkQl solutions and spreads. Will take another look at this after 15.10)*

The ±20% spread in maximum cavity operating gradient complicates the job of the LLRF controller since the relative forward power and Q_{ext} of each cavity must be individually tailored to its operating gradient and the beam current. This is necessary to achieve the required constant voltage of the individual cavities during the beam pulse, while maximising RF power efficiency. The detrimental effect of a mismatch is illustrated in Fig. 3.34, where all cavities have identical Q_{ext}. As the beam current is increased, the individual cavity voltages tilt up or down over the duration of the beam pulse, depending on whether they are operating at gradients above or below the mean gradient. An effect of the gradient tilts is to reduce the maximum achievable gradient vector-sum in the module.

The remote adjustability of cavity coupler (Q_{ext}) and the local power distribution system (P_k) provide the ability to tailor the RF conditions to achieve flat gradients in all cavities, for any given beam current [**?**]. (**Ed:** *NJW: need to provide comprehensive report on these solutions as a reference)* Furthermore, experiments at FLASH have demonstrated the ability of the LLRF system to automatically 'fine

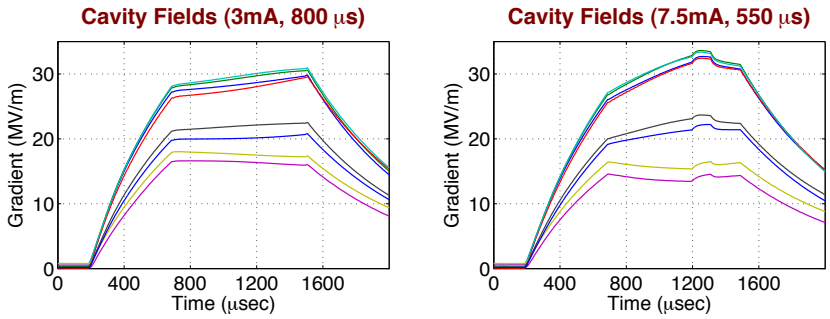

Figure 3.34. Cavity gradients for two beam loading conditions without $P_k Q_l$ optimisation

tune' the cavity voltage flatness by small incremental adjustments of the couplers (see Part I Section **??**).

3.7.4 LLRF operation

Besides implementing vector sum control, the central LLRF controller performs several other functions:

3.7.4.1 Exception handling

The LLRF system must detect and react to off-normal conditions that could be potentially damaging or could result in machine downtime. Depending on the severity of the condition, the response to the alarm condition might be to temporarily turn down the klystron output, turn off the rf drive until the next pulse, or turn off the rf drive and wait for operator intervention.

3.7.4.2 Automation

It will be essential to automate operation of the main linac llrf systems, if for no other reason the impracticability of manually performing the necessary operational functions. Examples of automation that are already routinely in operation or are under development at FLASH include: startup and shutdown of the rf systems; cavity resonance control, including compensation of Lorenz-forces; vector- sum calibration; quench detection; learning feedforward for the vector sum controller; drift compensation; Loaded-Q optimisation for flat gradients, etc.

3.7.4.3 Beam loading compensation

The forward power during the fill time is function of the required cavity fields, while the flat-top power is a function of both the cavity fields and the beam current. With the exception of the ideally matched case (no reflected power), the required forward power during the beam-on period is not the same as that required during the fill time. Since the beam current is already known a priori from the Damping ring instrumentation, the LLRF system can pre-emptively step the forward power to the

appropriate level immediately before the arrival of the first bunch. This is illustrated in Fig. 3.35, which shows the klystron forward power envelope for operation over a range of beam currents around the nominal design value. Without this feed-forward pre-programming of the RF power, there would be a transient perturbation on the cavity fields as the LLRF feedback system dynamically corrected the forward power.

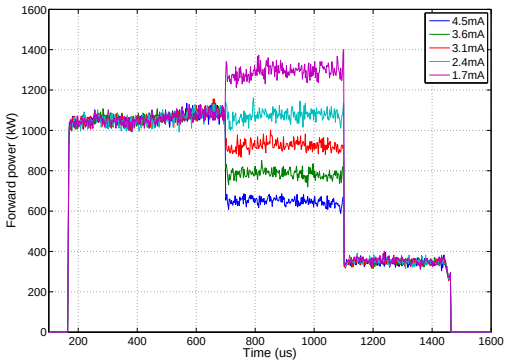

Figure 3.35. Klystron forward power for a range of beam currents

3.7.5 LLRF system implementation

A functional block diagram of the FLASH LLRF system is shown in Fig. 3.36.

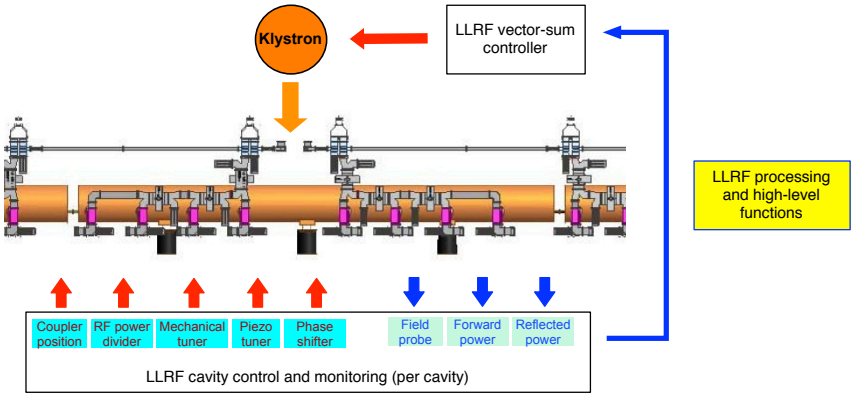

Figure 3.36. Overall layout of LLRF controller functions

To minimise distances over which RF signals must be transported, a distributed LLRF hardware architecture is used, similar to that used for the European XFEL. Front-end controllers are installed close to each cryomodule that contain the down-converters and digitisers for the field probes, forward and reflected power measurements for each of the cavities in the cryomodule. A partial cavity field vector sum is computed and transmitted in real time to the central vector sum controller. The front-end controller also drives the cavity mechanical tuners, piezo tuners, power distribution system power ratios, and cavity input couplers. Front-end controllers communicate with the vector sum controller and with serves via dedicated synchronous data links and fast Ethernet.

Algorithms that operate at the individual cavity level implemented in this front-end controller, including: optimisation of feed-forward drive parameters for each piezo tuner in order to compensate Lorentz- force detuning; P_k-Q_{ext} optimisation to flatten the cavity gradients during the beam-on period; and real-time computation of the Loaded-Q and detuning offsets for each cavity based on the field probe and forward/reflected power measurements.

Bibliography

[1] "TESLA Technical Design Report, March 2001. TESLA Report 2001-23" http://flash.desy.de/tesla/tesla_documentation/#e1509

[2] C. Pagani *et al.*, ["Construction, commissioning, and cryogenic performances of the first TESLA Test Facility (TTF) cryomodule,"] Adv. Cryogenic Eng. **43A** (1998) 87–97. http://wwwsrf.mi.infn.it/publications/papers/1998/file/cec97-1.pdf/

[3] T. H. Nicol, "TESLA test cell cryostat support post thermal and structural analysis," TESLA 94-12 (1994), http://flash.desy.de/reports_publications/tesla_reports/tesla_reports_1994/.

[4] C. Pagani *et al.*, ["Design of the thermal shields for the new improved version of the TESLA Test Facility (TTF) cryostat,"] Adv. Cryogenic Eng. **43A** (1998) 307–314. http://wwwsrf.mi.infn.it/publications/papers/1998/file/cec97-3.pdf

[5] K. Jensch, R. Lange, and B. Petersen, ["Numerical simulations for the cooldown of the XFEL and TTF superconducting linear accelerators,"] AIP Conf. Proc. **790** (Adv. Cryogenic Eng., **49A**) (2004) 371, DOI: 10.1063/1.1774705.

[6] M. Kemp *et al.*, "The SLAC P2 Marx," presented at the 2012 Power Modulator and High Voltage Conference, San Diego, CA, 2012. http://slac.stanford.edu/pubs/slacpubs/15000/slac-pub-15118.pdf

[7] K. Macken *et al.*, "A hierarchical control architecture for a PEBB-based ILC Marx modulator," SLAC-PUB-13744, *Proc. PPC'09, Washington, DC, 2009, pp. 826-831*, DOI: 10.1109/PPC.2009.5386259. http://ieeexplore.ieee.org/xpl/articleDetails.jsp?arnumber=5386259

[8] C. Nantista, C. Adolphsen, and Faya Wang, "Waveguide System R&D for the ILC Klystron Cluster Scheme," *Proc. LINAC 12, Tel-Aviv, Israel, Sep. 9-14, 2012, pp. xx (XX).*

[9] C. D. Nantista, W. R. Fowkes, N. M. Kroll and S. G. Tantawi, "Planar waveguide hybrids for very high power RF," arxiv:physics/0102033, *Proc. PAC 99, New York, NY, 1999, pp. 1432-1434 (TUA153)*, DOI: 10.1109/PAC.1999.795572.

[10] S. Fukuda *et al.*, "Status of RF Sources in Super-Conducting RF Test Facility (STF) at KEK," *Proc. PAC 09, Vancouver, BC, Canada, 2009, pp. 1032-1034 (TU5PFP086)*

(**Author:** *BL: Suggestions for more references)*

(**Author:** *References for blade tuner)*

[11] C. Pagani, A. Bosotti and R. Paparella, "WP8 - Blade Tuner Deliverable 8.2 : Report on Blade Tuner activity," ILC-HiGrade-Report-2010-001-1 (2010), `http://www.ilc-higrade.eu/e83212/e99561/e99563/ILC-HiGrade-2010-001-1.pdf`

[12] A. Bosotti, C. Pagani, N. Panzeri, and R. Paparella, "The Coaxial Blade Tuner – Final Report and Evaluation of Operation," CARE-Report-2008-018-SRF (2008). `http://irfu.cea.fr/Phocea/file.php?class=std&&file=Doc/Care/care-report-08-018.pdf`

[13] A. Bosotti *et al.*, "Full characterization of the Piezo Blade Tuner for superconducting RF cavities," *Proc. EPAC 08, Magazzini del Cotone, Italy, 2008, pp. 838-840 (MOPP120)*

[14] A. Bosotti, C. Pagani and N. Panzeri, "Improved Design of the ILC Blade Tuner for Large Scale Production," *Proc. PAC 07, Albuquerque, NM, 2007, pp. 2089 (WEPMN020)*, DOI: 10.1109/PAC.2007.4441159.

(**Author:** *Magnetic shield)*

[15] A. Koski and S. L. Wipf, ["Magnetic shielding of an accelerator beam using passive ferromagnetic material,"] IEEE Trans. Magnetics **32** (1996) 2663. DOI: 10.1109/20.511422

(**Author:** *Quadrupole)*

[16] V. S. Kashikhin *et al.*, "Superconducting splittable quadrupole magnet for linear accelerators," IEEE Trans. Appl. Supercond. **22** (2012) 4002904 (Proc. MT-22), DOI: 10.1109/TASC.2011.2176297.

[17] V. S. Kashikhin, "Novel Approach to Linear Accelerator Superconducting Magnet System," IEEE Trans. Appl. Supercond. **22** (2012) 4003904 . DOI: 10.1109/TASC.2011.2177236.

(**Author:** *Input coupler)*

[18] C. Adolphsen *et al.*, "SLAC/FNAL TTF3 Coupler Assembly and Processing Experience," *Proc. SRF 2011, Chicago, IL, 2011, pp. 476-478 (TUPO042).*

[19] M. Lacroix, F. Richard, L. Lukovac and W. Kaabi, "Coupler status," ILC-HiGrade-Report-2010-002-1 (2010). `http://www.ilc-higrade.eu/e83212/e99561/e99565/ILC-HiGrade-2010-002-1.pdf`

[20] H. Jenhani, T. Garvey and A. Variola, "RF conditioning studies of input power couplers for superconducting cavities operating in pulsed mode," Nucl. Instrum. Meth. A **595** (2008) 549-560. DOI: 10.1016/j.nima.2008.07.111

[21] B. Dwersteg *et al.*, "Tesla RF Power Couplers Development at DESY," *Proc. SRF 2001, Tsukuba, 2001, pp. 443-447 (PT001).*

[22] W.-D. Moeller [TESLA Collaboration], "High power coupler for the TESLA Test Facility," *Proc. SRF'99, Santa Fe, NM, 1999, pp. 577-581 (THA010).*

(**Author:** *HOM coupler references)*

[23] J. S. Sekutowicz, "HOM damping and power extraction from superconducting cavities," *Proc. LINAC 06, Knoxville, TN, 2006, pp. 506-510 (WE2005).*

[24] J. Sekutowicz, "Higher Order Mode Coupler for TESLA," *Proc. SRF'93, Newport News, VA, 1993, pp. 426-439 (SRF93G04).*

(**Ed:** *Start of MLTECH CRYOMOD references)*

[25] N. Ohuchi *et al.*, "Thermal performance of the S1-Global Cryomodule for ILC," *Proc. IPAC 2011, San Sebastian, Spain, 2011, pp. 2472-2474 (WEPO035)*

[26] X.L. Wang *et al.*, "Thermal performance analysis and measurements for the accelerator prototype modules of european XFEL," *Presented at the TESLA Technology Collaboration Meeting, IHEP, Bejing, China, 5-8 December, 2011* `http://indico.ihep.ac.cn/materialDisplay.py?contribId=25&sessionId=9&materialId=slides&confId=2240`

[27] V. S. Kashikhin *et al.*, "Superconducting splittable quadrupole magnet for Linear Accelerators," IEEE Trans. Appl. Supercond. **22** (2012) 4002904 (Proc. MT-22), DOI: 10.1109/TASC.2011.2176297.

[28] M. W. McGee, V. Vocean, C. Grimm and W. Schappert, "Transatlantic transport of Fermilab 3.9 GHz cryomodule for TTF/FLASH to DESY," *Proc. EPAC 08, Magazzini del Cotone, Italy, 2008, pp. 592-594 (MOPP022).*

[29] P. Pierini, B. List, "ILC cryomodule parameters," 2012, EDMS ID: D00000000973345.

[30] T. Peterson, B. List, "ILC SCRF cryogenics parameters for KCS," 2012, EDMS ID: D00000000975575.

[31] T. Peterson, B. List, A. Enomoto, "ILC SCRF cryogenics parameters for DKS," 2012, EDMS ID: D00000000991555.

[32] T. Peterson, "ILC cryogenic heat loads and cryoplant parameters," 2012, EDMS ID: D00000000994395.

[33] T. Peterson *et al.*, ["A survey of pressure vessel code compliance methods for superconducting radio frequency cryomodules,"] AIP Conf. Proc. 1434 (Adv. Cryogenic Eng. **57**), (2012) 1575-1582, DOI: 10.1063/1.4707088.

(**Ed:** *Start of MLTECH/LLRF-CONTROL references)*

[34] C. Schmidt *et al.*, "Feedback strategies for bunch arrival time stabilization at FLASH towards 10 fs," *Proc. FEL'11, Shanghai, China, 2011, pp. 531-534 (THPA26)*

[35] R. Carcagno *et al.*, "First Fermilab results of SRF cavity Lorentz force detuning compensation using a Piezo tuner," *Proc. SRF 2007, Beijing, China, 2007, pp. 259-263 (TUP57).*

[36] M. K. Grecki*et al.*, "Compensation of Lorentz force detuning for SC Linacs (with Piezo tuners)," *Proc. EPAC 08, Magazzini del Cotone, Italy, 2008, pp. 862-864 (MOPP129).*

[37] (**Author:** *L. Lilje - find reference to detuning measurement)* (**Ed:** *BL: Do you mean)* S. P. Sekalski *et al.*, "Static absolute force measurement for preloaded Piezoelements used for active Lorentz force detuning system," *Proc. LINAC 2004, Lübeck, Germany, 2004, pp. 486-488 (TUP89).*

[38] W. Schappert, Y.Pischalnikov and M. Scorrano [Project X Collaboration], "Resonance control in SRF cavities at FNAL," *Proc. PAC 11, New York, NY, 2011, pp. 2130-2132 (THOCS5)* [FERMILAB-CONF-11-143-TD].

[39] Toshiba Electron Tubes and Devices, with permission.

List of Figures

List of Tables